Pro Gradu

Transition-Edge Sensor Array Development

Mikko Palosaari

July 30, 2009

JYVÄSKYLÄ UNIVERSITY
NANOSCIENCE CENTER
DEPARTMENT OF PHYSICS
NANOPHYSICS

SUPERVISOR: Ilari Maasilta

Preface

The work reported in this Master's thesis has been done between July 2007 and July 2009 at Nanoscience Center at the Department of Physics in the University of Jyväskylä.

First, I would like to thank my supervisor Professor Ilari Maasilta, who has been an excellent advisor both in the experimental and theoretical work as well as in the writing process of this Master's thesis. In addition, I would like to thank him for the interesting research topic and the opportunity to work in his experimental nanophysics group. I would also like to thank Ph.D. student Kimmo Kinnunen for his valuable contribution to all the experiments, especially with low temperature measurements. Also without his know-how in sample fabrication, work behind this thesis would have been much more tedious. All in all he has helped me a lot in this project. The working atmosphere in Nanoscience Center has been enjoyable, for which I would like to thank the whole staff in the building.

Finally, I would like to thank my wife Suvi for always being there for me.

Jyväskylä 27th July 2009

Mikko Palosaari

Abstract

Transition Edge Sensors (TES) have been under heavy research in recent years thanks to their excellent energy resolution and high quantum efficiency. TES is based on the sharp transition between the superconductive and the normal state in superconductive thin films. When a single photon hits a TES its energy is converted into heat, which can be measured with this sensitive detector. TES was first developed to be used in space research for radiation detection. Nowadays they are finding new ground in other research areas thanks to their superior features and the fact that cooling techniques together with readout techniques have matured enough. The main motivation for our research is to develop TES arrays for detectors in e.g. X-ray absorption spectroscopy. The processing of TESs fabricated in Nanoscience Center in Jyväskylä are presented as well as the first 32 pixel TES array. In this thesis the basic properties of TESs like critical temperature and resistivity of the absorber material are under investigation. Also the use of ALD deposited insulator layer for the so-called Corbino-TES (CorTES) is discussed.

Transitioreunailmaisimia (TES) on tutkittu viime vuosien aikana paljon niiden erinomaisen energia resoluution sekä korkean suorituskykynsä ansiosta. TES-ilmaisimilla mitataan säteilyä ja niiden toiminta perustuu suprajohtavan- ja normaalitilan välillä tapahtuvaan herkkään vastuksen muutokseen suprajohtavissa ohutkalvoissa lämpötilan muuttuessa. Kun TES:iin osuu yksittäinen fotoni, sen energia muuttuu lämmöksi, joka voidaan mitata tällä herkällä ilmaisimella. Näin saadaan tietoa säteilyn spektristä erittäin tarkasti. Alun perin avaruustutkimukseen suunnitellut laitteet ovat alkaneet saada jalansijaa myös muilla tutkimusalueilla niiden erinomaisten ominaisuuksien ansiosta. Niiden resoluutio, tehokkuus ja lähivuosina tarpeeksi kehittyneet mittausjärjestelmät tekevät siitä halutun menetelmän useihin eri sovellutuksiin. Suurin motivaatio tämän työn takana on kehittää usean pikselin TES-matriiseja esim. röntgenabsorptiospektroskopiaa varten. Tässä työssä esitellään Jyväskylän yliopistossa Nanoscience Centerissä kehitettyjen TES:ien ominaisuuksia, kuten niiden kriittisiä lämpötiloja ja esim. absorberimateriaalin resistiivisyyttä. Työssä esitellään myös esimerkiksi ALD-menetelmällä tuotetun eristemateriaalin käyttö ns. Corbino-TES:ien (CorTES) valmistuksessa.

Contents

Chapter 1

Introduction

Superconducting transition edge sensors (TES) have been under heavy research in recent years. The need for ever better energy resolution radiation detectors drives the development of TESs. The ultimate goal for any spectrometer is to have high resolving power and throughput simultaneously over a wide energy range. Conventional silicon diode detectors used as X-ray detectors have good efficiency but their energy resolution is only 100 eV – 200 eV [1]. Wavelength dispersive spectrometers have resolution less than 10 eV but they have low throughputs. A TES detector working at around 100 mK can have resolution of about 2 eV at 6 keV [2] or even better with high efficiency.

The sensitivity of a TES comes from the fact that the sensor is operated between superconducting and normal states. The superconducting phase transition can be extremely sharp as a function of temperature, which indicates its use as a thermometer. The sensitivity of a TES can be two orders of magnitude larger than with conventional semiconductor thermistors [3].

The first demonstration of a TES was done in 1941, when a tantalum wire was operated in its superconducting transition and the increase of resistance caused by infrared signal was measured [4]. For 50 years after its invention TESs weren't really used in practical applications. Mainly this was due to the difficulty to match the noise of a TES to FET amplifiers [3]. Nowadays this problem has been eliminated by the use of a superconducting quantum interference device (SQUID) current amplifiers, which can be easily impedance-matched to low-resistance TES detectors [5].

Originally the driving force behind TES development were the needs of astrophysics research. Nowadays thanks to their superior combination of energy resolution and efficiency together with maturing readout and cooler technologies, TES based devices are now finding their way into new areas of research and applications.

Our group has started a collaboration with the chemical physics department in Lund University to use TES detectors in time resolved X-ray spectroscopy. With their expertise in X-ray absorption spectroscopy and our X-ray detectors integrated to the measurement system, our goal is to see chemical reactions of molecules in a way that has never been seen before.

The main theme of this thesis is to present the current state of the development of TES arrays in Nanoscience Center at the University of Jyväskylä.

In the second chapter the theory of basic superconductivity, the basics of TES theory and SQUID amplifiers are presented. Also different TES applications are introduced, especially time resolved X-ray spectroscopy. The third chapter holds everything about TESs studied in this thesis. The fourth chapter is about absorber element development and the fifth chapter concerns the ALD test. In the last chapter are the conclusions.

Chapter 2

Theory and Background

2.1 Superconductivity

Because superconductivity is such an important part of TESs it will be described here in an introductory manner.

The electrical resistivity of many metals and alloys drops suddenly to zero when a certain low enough temperature is reached, usually in the range of boiling point of liquid helium (4.2 K). The phenomenon is called superconductivity, which was first discovered by H. K. Onnes in 1911 when he measured the sudden drop of resistance in mercury, when it was cooled around to 4 K [6].

When the phase transition happens at the critical temperature T_c, the material goes from the normal state to the superconducting state. During this transition the resistance of a material becomes zero, but a superconductor is more than an ideal conductor. Another effect that relates to the superconducting state is the so–called Meissner effect, which means that the superconductor becomes a perfect diamagnet [7]. Because of this an external magnetic field can not penetrate inside the superconductor (Fig. 2.1).

For decades the theoretical description of superconductors was under investigation and in the 1950–1960s a very accurate theoretical picture of the classical superconductors emerged. But in 1986 a new class of high temperature superconductors were discovered by Bednorz and Müller [8]. The high temperature superconductors have the same general phenomenology as the classical superconductors, but the basic microscopical theory remains a mystery even today. The record for the highest transition temperature is for $HgBa_2Ca_2Cu_3O_{10}$ (HBCCO) : $T_c = 138$ K [9], while in classical superconductors the T_c is usually in the range of few Kelvins.

2.1.1 BCS Theory

The BCS theory (named after its creators, Bardeen, Cooper, and Schrieffer) explains the conventional superconductivity. It proposes that electrons with opposite spins can

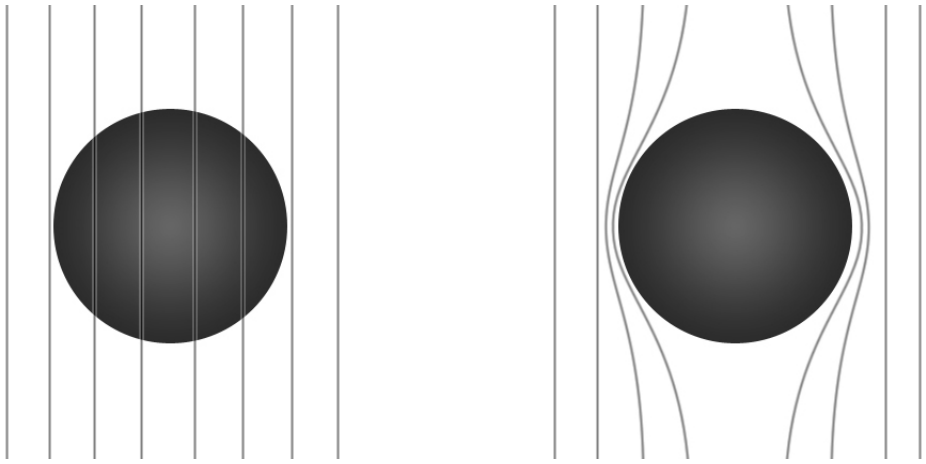

Figure 2.1: On the left is a ball made from superconducting material in an applied magnetic field and $T > T_C$. On the right $T < T_C$ and the magnetic field can't penetrate in the ball. Figure from S. Kulju.

form a so-called Cooper pair, even with a weak interaction, which leads into superconductivity. The authors received the Nobel Prize in Physics in 1972 for this theory.

The basic idea behind BCS theory is that one has to take the vibrations of ion cores into account to achieve a superconducting state. The physical idea is that a first electron (the polarizer) polarizes the medium by attracting positive ions; these excess positive ions in turn attract the second electron (the analyzer) giving an effective attraction interaction between electrons [10]. This phenomenon results in superconductivity if the attraction is strong enough to override the repulsive screened Coulomb interaction.

The attractive interaction between electrons results in a ground state separated from the excited states by an energy gap [7]. Most electromagnetic properties arise from this energy gap. The BCS theory does not apply to the high T_c superconductors.

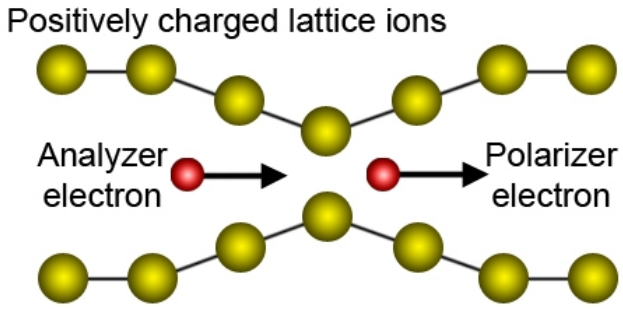

Figure 2.2: Cooper pair moving through lattice

Some other kind of mechanisms come to play in these temperatures, where the exchange particles may be other bosons than phonons. Soon after the publishing of BCS theory (1957) it was realized that a full treatment of both the charge and spin degrees of freedom of the electron predicts the existence of attractive components of the effective interaction between electrons even in the absence of lattice vibrations [11], especially with high-T_c superconductors.

BCS theory predicts some properties of classical superconductors that satisfy experiments. The isotope effect tells that the thermodynamical critical field H_c should scale as $M^{-1/2}$, where M is the isotopic mass of a superconductor. Also the BCS theory gives an estimate for the energy gap E_g at T = 0 K [12] to break a Cooper pair:

$$E_g = 2\Delta(0) = 3.528 k_B T_c, \tag{2.1}$$

where k_B is the Bolzmann constant, $\Delta(0)$ is the gap per quasiparticle and T_c is the transition temperature.

In BCS theory, the size of the Cooper pair wave function is determined by the temperature dependent coherence length $\xi(T)$, which at absolute zero has a value

$$\xi_0 \equiv \xi(0) \approx \frac{0.18 v_f}{k_B T_c}, \tag{2.2}$$

where v_f is the Fermi velocity of the material.

2.1.2 Ginzburg-Landau Theory

The BCS theory works well in cases where the energy gap is constant in space [10]. In case of spatial inhomogenity the microscopic theory becomes very difficult, and much reliance is placed on the macroscopic Ginzburg-Landau (GL) theory.

In GL theory a pseudowavefunction $\psi(r)$ is introduced as a complex order parameter $|\psi(r)|^2$ to represent the local density n_s of superconducting electrons. The theory was derived by applying variational principle to free-energy density in powers of $|\psi|^2$ and $|\nabla\psi|^2$. GL theory also naturally introduces a coherence length ξ, that measures the distance within which the superconducting Cooper pair concentration cannot change drastically [7].

One result of the GL theory is that the characteristics of a superconductor with applied magnetic flux (i.e. superconductor on its transition) are strongly dependent on its dimensionless Ginzburg-Landau parameter [3]

$$\kappa \equiv \frac{\lambda_{eff}(T)}{\xi(T)}, \tag{2.3}$$

where $\lambda_{eff}(T)$ is an effective temperature-dependent penetration depth. If $\kappa < 1/\sqrt{2}$ the superconductor is a type I superconductor otherwise it is type II superconductor.

2.1.3 Type I and Type II Superconductors

Superconductors are perfect diamagnets, but a strong magnetic field can destroy the superconductivity. The critical value of the magnetic field is $H_c(T)$, so it is a function of the temperature [7] and $H_c(T_c) = 0$. The phase transition and magnetization of the superconductor under the applied magnetic field can be seen in Fig. 2.3.

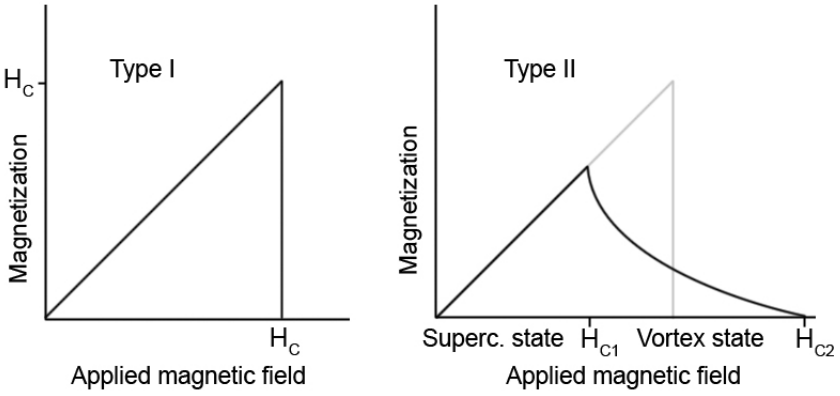

Figure 2.3: Magnetization of a type I and II superconductors in an applied magnetic field.

The difference between type II superconductors and type I is the different kind of Meissner effect. Although applied magnetic field H_c destroys the superconductivity in the type I superconductor it doesn't do it in the type II superconductor. For the type II superconductor there are two meaningful values, H_{c1} and H_{c2}.

The type II superconductor acts like the type I superconductor when applied field is weaker than H_{c1} (Fig. 2.3). When the magnetic field becomes stronger than H_{c1} the superconductor goes to a so–called vortex state. In this state some regions allow magnetic field to penetrate through the superconductor. These vortexes can form a 2-dimensional lattice (for example triangle) [7] on the surface of the superconductor. The superconductor is in this state until the applied field reaches the value H_{c2}. At that point the superconducting state will be destroyed and the type II superconductor goes to normal state.

A property telling a lot about a material is the mean free path of conduction electrons in the normal state. When it is long, the coherence length ξ is long. If $\xi > \sqrt{2}\lambda$ the material is a type I superconductor (see equation (2.3)). If $\xi < \sqrt{2}\lambda$, the material is type II superconductor. Materials can be changed from type I to type II by applying an alloying element. In this case there are no dramatical changes in critical temperature or electronic structure, but magnetic behavior transforms drastically [7]. In the case of thin films one should note that the dependence of ξ on mean free path can lead to type II behaviour for materials that are really type I in bulk.

2.2 TES Theory

2.2.1 Basic Concepts

Calorimeter is an instrument that measures energy and a bolometer is an instrument that measures power. A quantum calorimeter measures the energy of single quanta of light. In this section the principles and the basic equations needed to describe a simple calorimeter are discussed. TES detectors can be used as ultrasensitive calorimeters or bolometers.

In Fig. 2.4 a simple calorimeter (bolometer) is presented schematically. An absorber with heat capacity C is connected via weak thermal link with thermal conductance G to a heat sink (or cold bath) at temperature T_{bath}. Without external power an equilibrium is reached and the temperature $T(t)$ of the absorber will be the same as T_{bath}.

If a photon with energy E_γ is absorbed, the temperature of the absorber will rise and then cool back to the bath temperature. The same configuration can also be used to measure steady power input P as a bolometer. The difference is that while a calorimeter measures the energy of a single photon or particle a bolometer measures the flux of energy created by many photons or particles hitting the absorber in rapid succession.

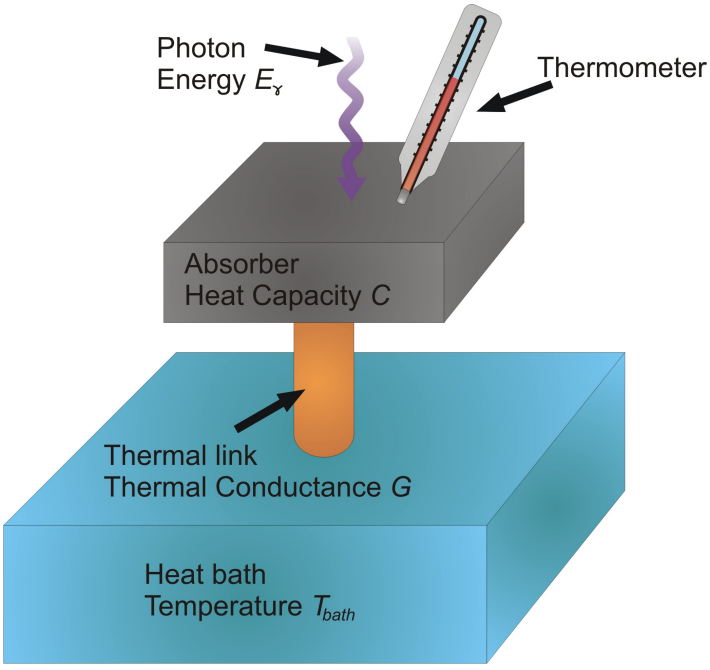

Figure 2.4: Schematical figure of a calorimeter. Incoming photon is absorbed and its energy is converted into heat. The heat increases the resistance of the TES from which one can deduce the energy of the absorbed photon.

In our case the thermometer is a superconducting thin film operated in its transition between the normal state and the superconducting state, hence the name supercon-

ducting transition-edge sensor. The transition temperature is usually about 100 mK. By operating microcalorimeters at low ($\sim$ 100 mK) temperatures, it is possible to simultaneously reduce the thermodynamic noise while increasing the thermal signal by reducing the heat capacity of the absorber, since the heat capacities of materials also drop at low temperatures [13]. The transition can be extremely sharp, which is described with the parameter

$$\alpha = \frac{\mathrm{d}\ \log\ R}{\mathrm{d}\ \log\ T}. \tag{2.4}$$

Sensitivity of the TES as a function of current is

$$\beta = \frac{\mathrm{d}\ \log\ R}{\mathrm{d}\ \log\ I}. \tag{2.5}$$

With these parameters the resistance of a TES can be approximated for small signals with the following equation

$$R(T, I) \approx R_0 + \alpha \frac{R_0}{T_0}\delta T + \beta \frac{R_0}{I_0}\delta I, \tag{2.6}$$

where R_0, I_0 and T_0 are the steady state TES resistance, current and temperature. The α of a TES can be two orders of magnitude larger than with conventional semiconductor thermistor thermometers [3].

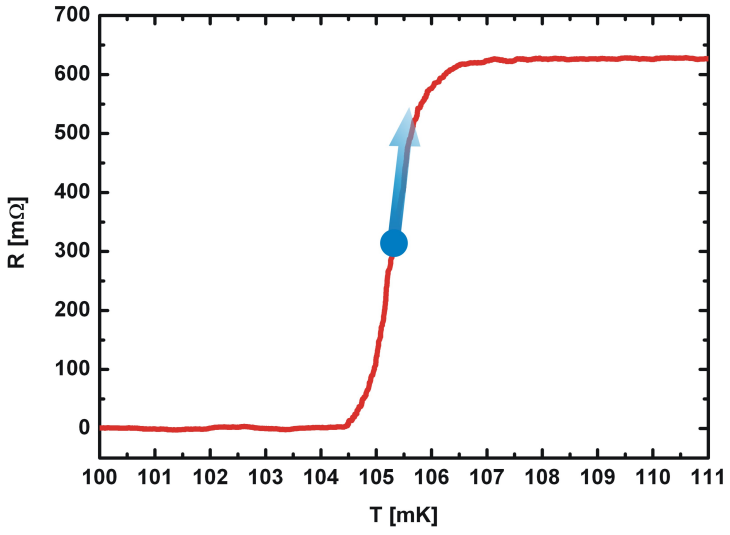

Figure 2.5: Basic operation of a TES. When a photon hits the absorber the temperature of the TES film is increased and the resistance of the system is changed.

When a constant power P is applied, the temperature of the absorber will rise above T_{bath} until the power flowing into the absorber equals the outflowing power to

the heatbath, P_{link}. The system can be modeled with a thermal equation [14]

$$C\frac{\mathrm{d}T(t)}{\mathrm{d}t} = P - P_{link}\left(T(t), T_{bath}\right) + E_\gamma \delta\left(t - t\gamma\right), \tag{2.7}$$

where $E_\gamma \delta\left(t - t\gamma\right)$ is the absorption event at time t_γ modelled with Dirac delta function. P_{link} depends on the particular device and will now be assumed to have the form

$$P_{link}\left(T(t), T_{bath}\right) = G(T(t) - T_{bath}). \tag{2.8}$$

Lets now set $t_\gamma = 0$ and insert equation (2.8) into (2.7):

$$C\frac{\mathrm{d}T(t)}{\mathrm{d}t} = P - GT(t) + GT_{bath} + E_\gamma \delta(t). \tag{2.9}$$

This equation is now linear and can be solved easily (Appendix B) to get

$$T(t) = \frac{E_\gamma}{C}\mathrm{e}^{-t/\tau} + \left(\frac{P}{G} + T_{bath}\right), \tag{2.10}$$

where $\tau = C/G$ is the time constant of the system and the constant part represents the steady state temperature. This means that the simplest calorimeter has an exponential decay response with time constant C/G and an initial temperature rise $\Delta T = E\gamma/C$ as in Fig. 2.6.

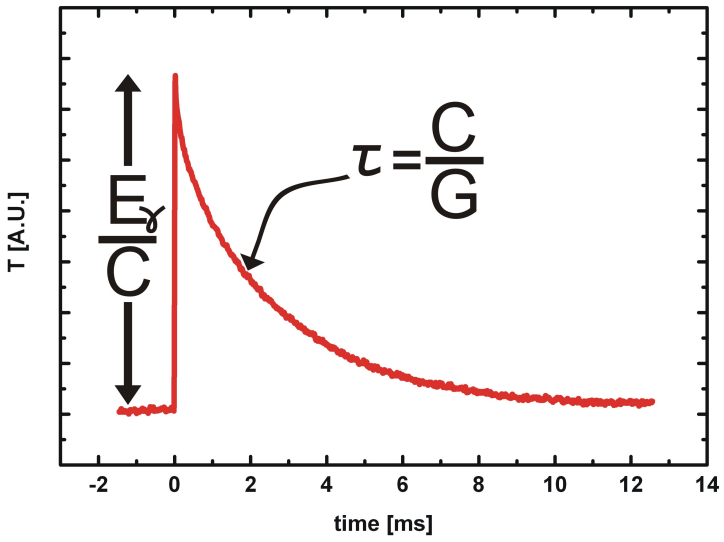

Figure 2.6: Exponential decay after absorption event of a photon.

In the above calculation it was assumed that the photon thermalizes immediately after absorption. In reality this is not the case of course. When an photon with energy

in the range of 1 keV – 10 keV hits the absorption material the main process that creates a signal in the thermometer is the creation of a photoelectron [14], where a bound electron is ejected from the atom. This electron has very short mean free path and it collides with other electrons releasing its energy. Soon the energy is spread out to a large number of energetic electrons via electron-electron interactions. The energy of all the particles in the detector rises and higher mean energy is reached. Eventually these electrons reach a thermal equilibrium with each other, in other words thermalization occurs, and temperature of the detector increases because of the increase of the mean energy.

2.2.2 Electrothermal Feedback

How to easily keep the TES in its transition and to make it come back to its operation point after an energy pulse was first demonstrated by Irwin [17]. The method is the so-called electrothermal feedback (ETF) and it is achieved by voltage biasing the TES. If the detector is voltage biased, Joule heating keeps the TES in its transition. This happens because with constant voltage the power input is

$$P(T) = \frac{V^2}{R(T)}. \tag{2.11}$$

When the TES is in the transition and the temperature increases the resistance of the TES also increases. This means that the heating power decreases, which then cools down the TES. So somewhere in the transition the input power and the power flowing to cold bath are equal and the TES finds an equilibrium and it wants to stay there. The effect is the negative ETF. As well as stabilizing the TES the negative ETF has also other benefits. For example it shortens the duration of pulses, which makes it possible to measure with higher count rates [14]. With the ETF the effective time constant is (with ideal voltage bias)

$$\tau_{eff} = \tau \frac{1+\beta}{1+\beta+\mathscr{L}}, \tag{2.12}$$

where

$$\mathscr{L} = \frac{\alpha I_0^2 R_0}{G T_0} \tag{2.13}$$

is the loop gain.

2.2.3 Noise

One irreducible source of noise comes from the random exchange of energy between the absorber and the heat sink over the thermal link [15]. The magnitude of the fluctuations in the energy content of the calorimeter results from classical statistical mechanics and is given by

$$< \Delta E^2 >= k_B T^2 C, \tag{2.14}$$

where k_B is the Bolzmann constant. From equation (2.14) one can see that these fluctutations do not depend on the thermal conductance G of the link.

One way to explain the basic noises is to use a block element model as in Fig. 2.7. The phonon noise or thermodynamic fluctuation noise (TFN) (eq. (2.14)) comes from the energy fluctuations between the TES and the heat bath through the weak thermal link with thermal conductance G. Internal thermal fluctuation noise (ITFN) arises, when an additional element (eg. absorber) is introduced to the system (as in Fig. 2.7) or because fluctuarions inside a TES film due to temperature gradients [16]. Then energy fluctuations between the TES and the additional element are seen as a new noise source. Thermal link G_{TES} determines the frequency at which the additional element decouples thermally from the TES. The associated time constant is given by

$$\tau_{de} = \frac{C_{de}}{G_{TES}}. \tag{2.15}$$

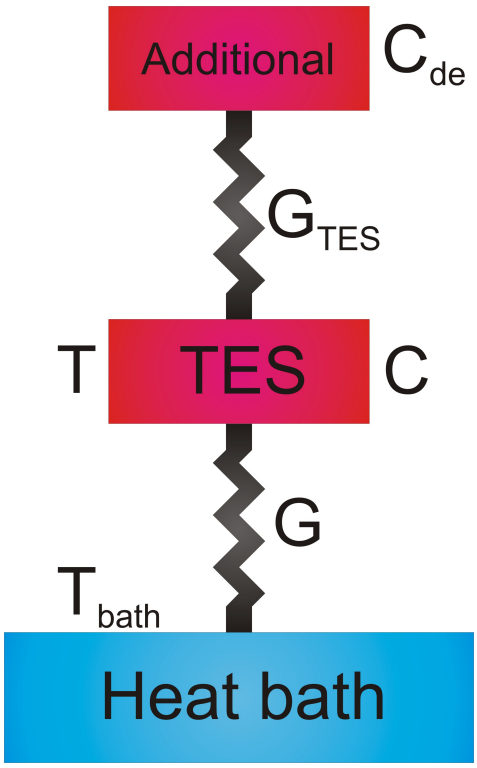

Figure 2.7: Thermical block diagram of TES with additional element eg. absorber.

Another fundamental noise source is the Johnson noise of the TES and other resistive elements (shunt resitor). This noise has the form of voltage source with spectral density $\sqrt{4k_BTR}$. But the TES in its transition is not a conventional resistor because its resistance is also a function of current as well as temperature. This leads into

non-linearities that have to be taken into account when doing a full theoretical treatment. In other words this means that some kind of quadratic expansions have to be considered [3].

When considering just phonon noise and Johnson noise the full width at half maximum (FWHM) energy resolution of a TES can be expressed with the formula, when $T_0 >> T_{bath}$ [17]

$$\Delta E_{FWHM} = 2.36 \times \sqrt{4k_B T_0^2 C \frac{1}{\alpha} \sqrt{\frac{n}{2}}}, \tag{2.16}$$

where n is the exponent of power flow equation

$$P = K(T_0^n - T_{bath}^n), \tag{2.17}$$

whose value depends on the dominant thermal impedance between the substrate and the electrons in the superconducting film [17]. K in eq. (2.17) is a material dependent parameter.

Readout noise is one noise source that always comes into play in real applications. The noise of SQUID amplifier is usually modelled with a white noise source. This noise source has only a small contribution to the total noise. In our setup this is 4 pA/$\sqrt{\text{Hz}}$.

In addition to these basic noise sources many groups have seen some "excess noise" that limits the resolution of TESs. This noise has been under investigation for quite some time in the TES field and different explanations have been suggested: Fluctuation superconductivity noise (FSN) is fluctuation-induced superconductivity above T_c near the normal metal – superconductor boundary [18], flux flow noise (FFN) that is generated by vortices moving inside the TES perpendicular to the current [19], percolation noise, which arises from superconducting domains randomly linking together [20] and non-equilibrium thermodynamics [21] to name a few. But now very recent work done in our group suggests that the "excess noise" is not excess but arises when the interactions between the TES and additional elements is treated carefully with the correct thermal model [22]. This thermal model can be probed by measuring the complex impedance of the system [23].

Noise equivalent power (NEP) is a concept that is useful, when theoretical resolution of a detector is determined. The NEP is the equivalent input power needed to produce a given output noise. When several noise mechanisms are in the system the NEP of each noise term can be determined individually and then the total NEP is the sum in quadrature of these separate terms [14].

By measuring the frequency-dependent complex electrical impedance Z of a detector, one can gain information also on the thermal circuit, if the detector is biased within the transition [22]. In the simplest case (as in Fig. 2.4) the frequency dependent complex impedance traces a semicircle in the complex plane (Fig. 2.8 upper figure, dotted green line). When additional thermal elements are included (as in Fig. 2.7) the

Z developes bulges at intermediate frequencies determined by the values of the additional heat capacities and thermal conductances to the TES (Fig. 2.8 upper image, red line).

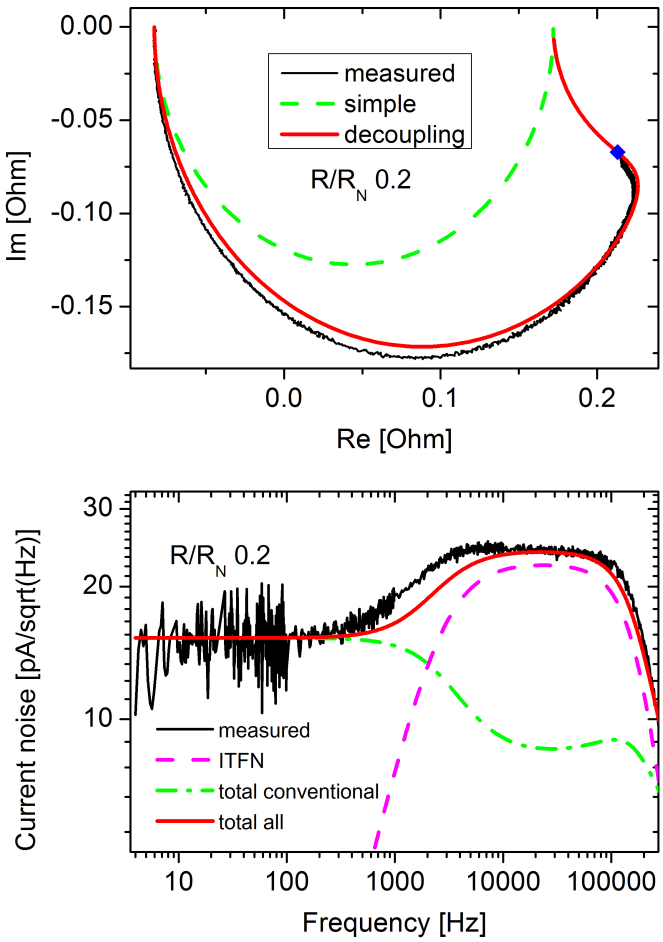

Figure 2.8: Complex impedance and current noise of a TES. Red curve in the upper image calculated with one additional element in the thermal model. Noise models calculated using parameters derived from the Z-models in the upper image. Data from [22].

One can see that the decoupled Z-fit in the Fig. 2.8 is not perfect compared to measured Z and most likely a third thermal element would be needed to explain the data fully.

2.3 SQUID

Superconducting quantum interference device (SQUID) is a device that utilizes a superconducting loop with two Josephson junctions. The Josephson phenomenon is derived in detail in Appendix A.

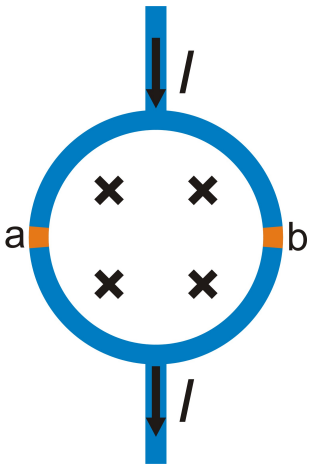

Figure 2.9: Schematical figure of a SQUID. Blue represent a superconductor and orange an insulator. X represents the magnetic field and I the current.

The general configuration of a DC SQUID is shown in Fig 2.9. A supercurrent is flowing along the two paths of a superconductor where both paths contain a tunneling barrier forming a Josephson junction. The supercurrents before and after the division are the same except for a phase differences δ_a and δ_b, which occur at the junctions a and b respectively. A magnetic field through the loop causes further shifts in the phase, which results in a periodic modulation of the supercurrent with changing magnetic field.

Supercurrents across the tunnel junctions a and b (Fig 2.9) can be written as

$$I_{a,b} = Aj_0 \sin \delta_{a,b}, \tag{2.18}$$

where A is the junction area and j_0 is the current density. Introducing a arbitrary phase factor δ_0 the individual junction phase shifts can be written as

$$\delta_a = \delta_0 + \frac{e}{\hbar}\Phi, \tag{2.19}$$

$$\delta_b = \delta_0 - \frac{e}{\hbar}\Phi, \tag{2.20}$$

where e is the electron charge, $\hbar$ is Plancks constant divided by 2π and Φ is the magnetic flux threading the loop. The supercurrent flowing through a SQUID can be shown [24] to be determined by the extent of a magnetic flux threading the device.

The supercurrent is given by:

$$I = 2Aj_0 \cos\left(\frac{e\Phi}{\hbar}\right) \sin\delta_0. \tag{2.21}$$

SQUIDs can be used as extremely sensitive magnetometers or ammeters. They are sensitive enough to measure fields as low as $5 \cdot 10^{-18}$ T within a few days of averaged measurements [25]. For reference, the Earth's magnetic field is in the range of 30 μT – 60 μT [26]. When used as an ammeter a current produces a magnetic flux through the SQUID, which can be measured with extreme accuracy.

2.4 TES Applications

As discussed before the TES was initially developed for the needs of astrophysical measurements. Nowadays they are being used in wide photon energy range to detect different kind of radiation. For example TESs are used as sub-mm cameras at the south pole and Chile for cosmic microwave background measurement [27], in quantum cryptography to detect single near-infrared photons [28], for gamma-ray detection in nuclear physics [29], for THz imaging of concealed weapons [30] and in the future for X-ray imaging spectrometry in collaboration with ESA, NASA and JAXA. One application that we may soon be involved with is particle-induced X-ray emission (PIXE), which is a technique to determine elemental make-up of materials. Other future application with TESs is X-ray absorption spectroscopy, in which our detectors will be used together with X-ray source from Lund University. This technique will be next discussed in detail.

2.4.1 X-ray Absorption Spectroscopy

X-ray absorption spectroscopy (XAS) is a powerful structural technique that allows one to investigate the neighborhood of a particular element embedded in a condensed medium [31]. It measures the absorption of X-rays as a function of the energy of the X-rays. More specifically, the X-ray absorption coefficient $\mu(E) = -\frac{\mathrm{d}\ \ln I}{dx}$ is determined from the decay in the X-ray beam intensity I with distance x. So the intensity I of the incoming X-ray decays exponentially as a function of distance in the medium.

When the absorption coefficient is plotted as a function of energy one can distinguish three different features (Fig. 2.10):

1. Overall decrease in X-ray absorption with increasing energy.
2. Sharp step-function like rise at certain energies, so-called edges.
3. Oscillatory structure above the edges that modulate the absorption typically by a few percent of the overall absorption cross section.

The first feature arises from quantum mechanical phenomenon of X-ray absorption by atoms, which can be explained for example with Fermi's golden rule. The energy position of the second feature comes from the excitation of inner-shell electrons to free or unoccupied continuum levels and it is unique to the absorption atom. The transition is always to unoccupied states and the transition leaves a core hole behind. The resulting excited electron is referred to as photoelectron and in a solid it generally has enough kinetic energy to move freely through the material. The naming of the edges (K,L_1,L_2 etc.) reflects the origin of the photoelectron e.g. K edge is a transition of the innermost $1s$ electron and therefore requires the most energy. The third feature

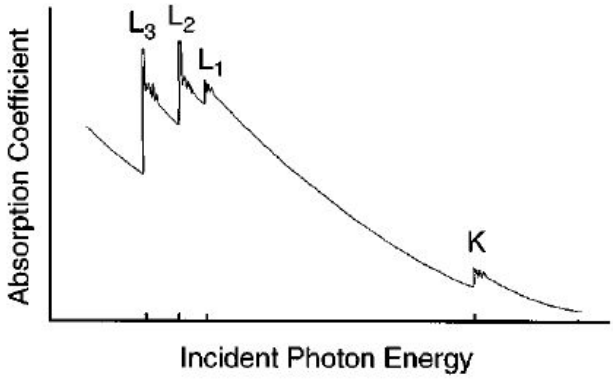

Figure 2.10: Schematics of X-ray absorption coefficient as a function of incident photon energy(adapted from [32]).

contains information about interatomic distances and coordination numbers and it is called X-ray absorption fine structure.

X-ray absorption fine structure (XAFS) refers to the oscillatory structure in the X-ray absorption coefficient just above an X-ray absorption edge [32]. XAFS is a fingerprint of a given material, which gives detailed information about atomic structure and electronic and vibrational properties of the material. Fine structure in the absorption well above an X-ray edge, the so–called extended XAFS (EXAFS), is now understood in terms of a high-order multiple-scattering theory. Region closer to an edge is often dominated by strong scattering processes as well as local atomic resonances in the X-ray absorption and is generally not as readily interpreted as EXAFS [32]. This strong scattering region is called X-ray absorption near-edge structure (XANES).

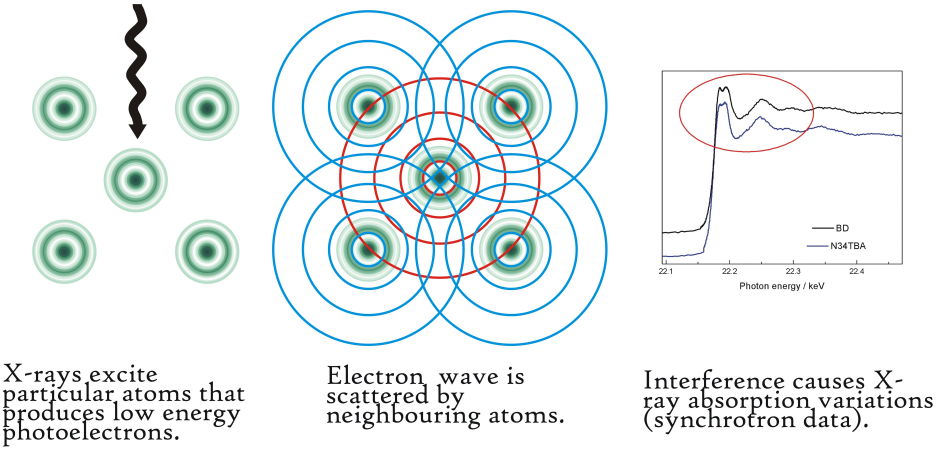

Figure 2.11: Schematical view for the origin of XAFS

The dominant wiggles in XAFS spectrum are interpreted as interference of the outgoing photoelectron quantum wave (Fig. 2.11). As the wave is reflected back from

neighbouring atoms the amplitude of all the reflected waves at the absorbing atom add either constructively or destructively to the outgoing photoelectron which will consequently modulate the absorption. Because the interference pattern depends on the energy of the photoelectron the absorption spectrum will have modulations to it. The photoelectron wave decays as a function of time and distance due to primarily inelastic losses and so XAFS can only give information on the local atomic structure (say of the order of nanometers [32]). It was only in the early 1970s when it was widely recognized that these interference patterns could used to obtain information on the local structure near an absorbing atom [33].

Usually the X-ray source for X-ray absorption spectroscopy is performed using synchrotron accelerator. This method is rather expensive and cumbersome. A chemical physics research group led by Villy Sundström at Lund University in Sweden has developed a new type of X-ray source that uses plasma created by femtosecond-laser [34]. With the setup in Fig. 2.12 one could do time resolved X-ray spectroscopy.

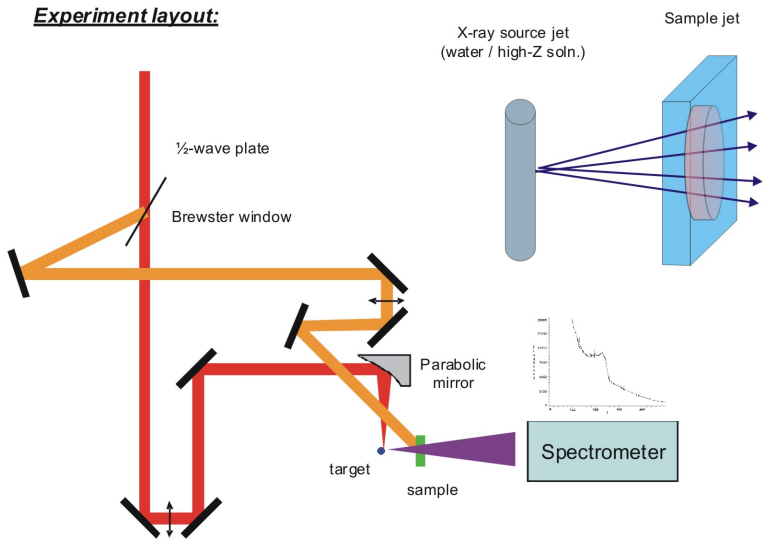

Figure 2.12: Setup for time resolved X-ray spectroscopy with the help of femtosecond laser pulse generated X-ray pulses. The red laser beam generates ultrashort X-ray pulses in a water jet and the orange laser beam initiates the chemical reaction in the sample. Image from V. Sundström.

Our group is doing collaboration with them, where our task is to develop TES arrays for the measurement setup to detect the X-ray absorption spectrum. With this combination time resolved chemical reactions of molecules can be seen in a way that has never been done before. For example the reactions of artificial photosynthesis (Fig. 2.13) could be one area of interest.

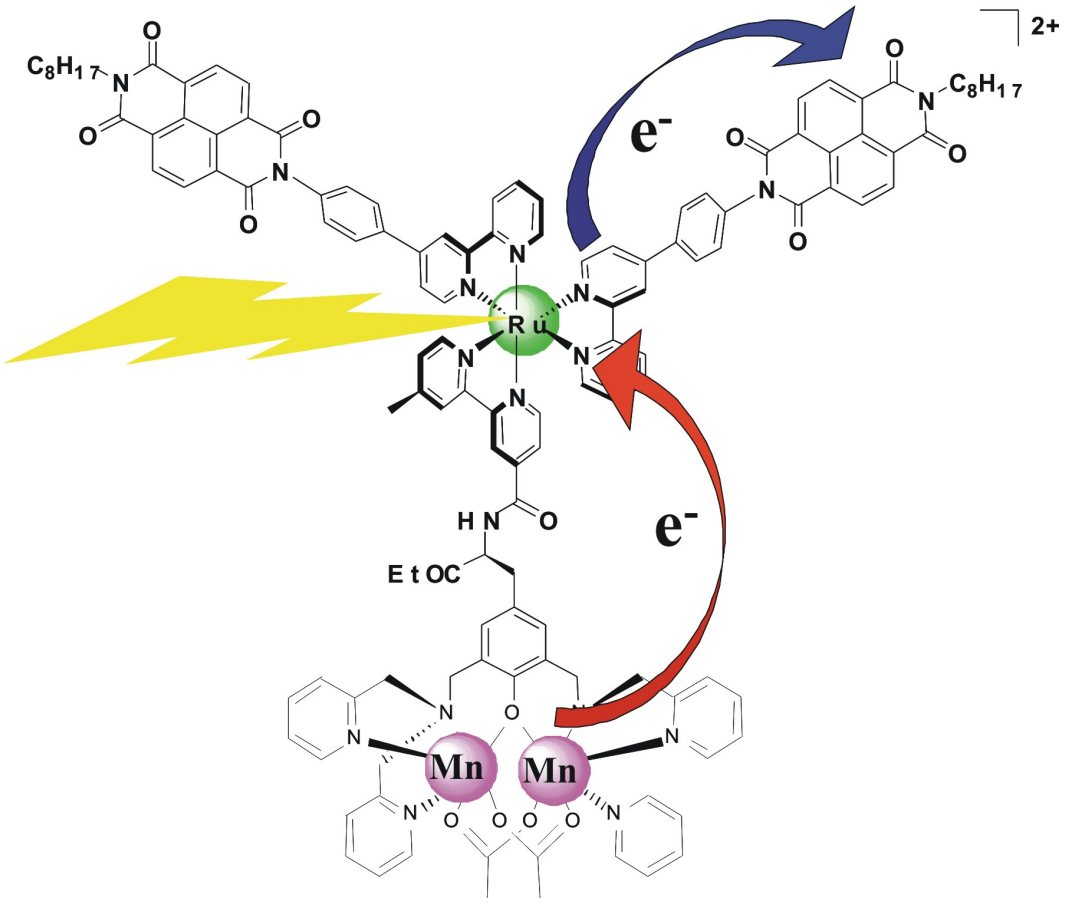

Figure 2.13: Multichromophoric molecule for artificial photosynthesis. Light absorption of the Ruthenium center starts electron transfer from the Mn-center to the Ru-center (red arrow), followed by electron transfer from the Ru-center to the aromatic units (blue arrow). By time resolved X-ray spectroscopy the light induced oxidation and reduction, as well as ensuing structural changes, can be monitored. Image from V. Sundström.

Chapter 3

TES Experiments

3.1 TES Structure

At the heart of every TES is the actual superconducting thin film. In our case we use a bilayer of gold and titanium. The critical temperature of titanium is ~ 400 mK but as we want to have the T_c around 100 mK we use the so-called proximity effect [35] to lower the T_c. In proximity effect a thin film of superconductor can have a lower critical temperature when a normal metal, gold in our case, is in contact with it and the thickness of the superconducting film is less than the coherence length $\xi(T)$ of the superconductor [3]. In practice we have about 40 nm of titanium with about 45 nm of gold on top of it, which are just empirically found parameters. There are some theoretical models for transition temperatures of proximity effect thin films [36], but they also need some empirical parameters. Another way to lower the T_c is to implant magnetical impurities (100 – 1000 ppm) into a superconductor. Then the thickness of the superconductor could be tuned to achieve a desired resistance of the normal state, but other diffuculties arise e.g. effects on the heat capacities [3].

To isolate a TES from its surrounding one needs to make the heat flow between the TES and the substrate as low as possible. Energy transport has to be optimized between them. In normal metals electrons carry most of the heat, but in superconductors and in insulators phonons do the job. So one has to restrict phonon transport from the substrate to the TES. This is usually done with a thin Si_3Ni_4-membrane on top of silicon substrate where silicon is etched away under the silicon nitride. The size of the membrane was chosen to be less than two times bigger than the area of the TES. If the membrane is diffusive the thermal conductance of the membrane depends on the size of it, but in ballistic case it does not.

The absorber transfers the energy of the incident photon and converts it into heat. A good absorber absorbs photons efficiently, has low heat capacitance C and high thermal conductance G [37]. A low C is desired because extra heat capacitance lowers the sensitivity and increases noise [3]. Bismuth's large atomic number and low carrier density makes it an attractive X-ray absorber material for microcalorimeters. It has

low heat capacity and good X-ray stopping power [38]. We use bismuth as absorbing material although it has rather poor thermal conductance because it is a semimetal. To ensure rapid thermalization of the deposited energy in the lateral direction, thin layers ($\sim$ 100 nm) of copper are used inside the absorber.

The leads that connect the TES to measurement setup are made of niobium, which is a superconductor and has a bulk T_c of 9.25 K. In thin films the T_c is usually less than the bulk value but with Nb it is still above liquid helium temperatures 4.2 K. So in any case the leads are superconducting in the operating temperature and do not dissipate any power or conduct any heat.

There are basically two types of TESs that we have been developing in our group. The first and the more simple one is so-called square-TES, where the geometry of the TES is rectangular. It takes 3 processing round to make it complete. The other type is the Corbino-TES (CorTES), where the geometry is circular. It takes five processing rounds to complete. Both TESs are presented in Fig. 3.1 In the CorTES the current

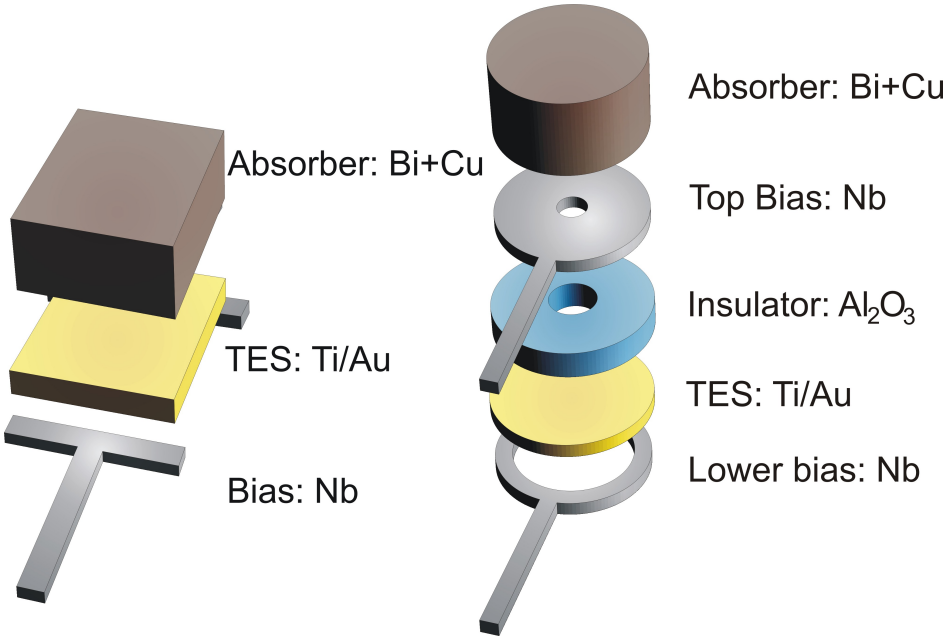

Figure 3.1: Schematical images of a square-TES and a CorTES.

flows radially from the top bias to lower bias. The lower bias contacts the outer rim of the TES film, while the top bias contacts the center of the TES. Also we have made three types of CorTESs, where the TES-film has been sliced in different ways (Fig. 3.2). This is done in order to see if the slicing has some effect in lowering the excess noise in a TES. There are some results about this property [39], but more research is needed. Also because the upper bias is superconducting and it covers almost the whole TES film it acts as a shield against external magnetic fields (Meissner effect), which may enhance the performance of the device.

The insulating layer in the CorTESs has usually been Al_2O_3. Because it has been made with electron beam vacuum evaporator, the thickness of the layer has been quite thick (> 100 nm) to prevent any pinholes.

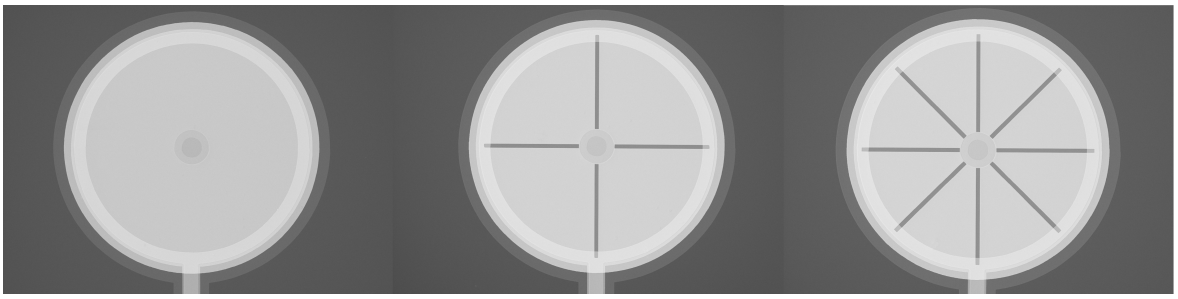

Figure 3.2: SEM images of different CorTESs. Left: OTES, Center: STES, Right: XTES. Notice that no absorber is deposited.

3.2 TES Array

In real applications a single pixel TES is often not enough, but an array of TESs is needed. With more pixels more events can be recorded simultaneously, but it also introduces complexity to the measurements e.g. multiplexing is needed. With many pixels there is a greater chance for capturing photons and usually a high filling factor of the pixels is desired. With TES arrays the uniformity of the pixels is essential, so that they all will work identically. For example the α, β and T_c should be the same with all the pixels. Kilopixel TES arrays have been demonstrated for example with the Atacama Cosmology Telescope [40].

In our EXAFS project with Lund University the pixel size will be about 250. The pixels will not require a large filling factor due to the nature of the X-ray source, which makes the fabrication of the array somewhat easier. The energy range of the incoming X-rays will be 2 keV – 10 keV.

3.3 Making of TESs

The samples were fabricated in Nanoscience Center at the University of Jyväskylä. Basic electron beam and photo lithography were used as fabrication methods, which are described by many authors e.g. [41], [42], [43] and also in my Bachelor's thesis [44].

3.3.1 Si_3N_4 Membrane Fabrication

As all the TESs are fabricated on Si_3N_4 membranes these had to be fabricated first. First a 300 µm thick silicon wafer (100) covered with 300 nm silicon nitride layers on

both sides was sliced in approriate sizes. For a single TES the size of the chip was approximately 1 cm × 0.7 cm and for the TES-array the size was about twice the size of the single TES chip.

After the cutting the chips were cleaned of silicon dust and other residues. The chips were immersed in boiling acetone and then sonicated for couple of minutes. Next the surfaces of the chips were rubbed with cotton sticks and then they were rinsed with isopropanol. When the surfaces were clean, the chips were blow dried using N_2-gas.

Once the cleansing was done the chips were covered with a resist on both sides. The resist used was AZ1415H photoresist. A couple of drops of liquid resist was dropped on the chip with a Pasteur–pipette. Then the chips were spinned with 4000 rpm for 1 minute in a spinner. After the spinning the chips were baked on a hot plate for 1 minute at 100 °C to solidify the resist. If the humidity of the cleanroom was higher than normal (say in summertime) the chips were also prebaked to guarantee proper development of the resist after exposure.

Before photo exposure a mask had to be made. The masks were made on a glass plate, which had a few hundred nanometers thick chrome layer on top. The pattern in the mask was wet etched with chromium etchant with the help of PMMA resist layer. The pattern in the resist was done with e-beam lithography.

The exposure was done with Karl Suss mask aligner. The samples and the mask were aligned first and the samples were exposed for 70 s with UV-light.

After exposure the samples were developed with AZ351B developer (mainly buffered NaOH). Next they were dry etched with Reactive Ion Etcher (RIE) to remove the silicon nitride layer from the parts were there was no resist. RIE is a plasma-based dry etching technique characterized by a combination of physical sputtering with chemical activity of reactive species. This enables the achievement of material selective etch anisotropy [45] and makes it more selective than sputtering and more directional than plain plasma etching.

The silicon nitride layer was dry etched from the exposed area with CHF_3-gas in O_2 atmosphere at 30° C with 150W RF-Power. The etching rate was 50 nm/min and the thickness of the nitride layer was 300 nm, hence the etching time was set to seven minutes just to be sure that all the nitride was etched. CHF_3-process is selective against silicon and it results in anisotropic profiles unlike SF_6- or CF_4-based processes [46].

When the silicon nitride was etched away, the rest of the resist was dissolved with acetone. Next the samples were put in a container with KOH in it. Then the container was put in a heat bath of boiling water. KOH etches (100) silicon in 54.7 degree angle. For 300 μm it takes a few hours to etch the silicon away at 100 °C.

When the wet etching was done the samples were rinsed in hot water several times, after which the membranes were complete. Schematical figure of the processes in Fig. 3.3.

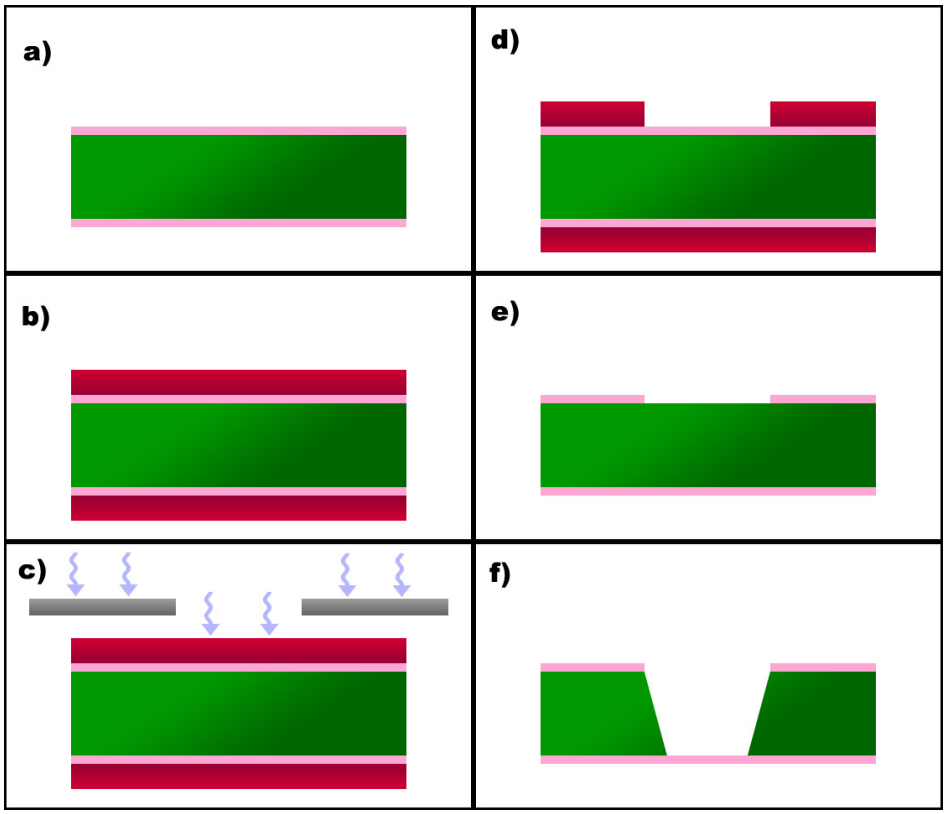

Figure 3.3: Schematical figure of making of the Si_3N_4-membrane. a) Silicon substrate with Si_3N_4-thin film on top. b) Deposition of photoresist. c) UV exposure through mask d) Development of the photoresist. e) Dry etching of Si_3N_4:n with RIE. f) Wet etching of silicon in KOH.

3.3.2 TES Fabrication

When the substrate and its silicon nitride membranes were made the actual processing of the TES could be done. Now processing was done with electron beam lithography, where instead of UV light one uses a beam of electrons to write patterns. The method is well suited for research because of smaller line widths and it is a very flexible method (e.g. no masks are needed).

3.3.3 Resists

A double layer resist was used with every processing round except for the making of the absorber, where a thicker one-layer resist was used. A double layer makes the lift-off process easier. Resists were deposited in a spinner and baked on a hot plate at 160 °C to solidify the resist. After spinning the thick resist layer for the lithography of the absorber the samples were stored overnight to get all moisture out of the resist, which reduces charging of the resist during e-beam lithography. Parameters for the deposition of resists are in table 3.1.

Table 3.1: Resist parameters

	Resist	Spinning [rpm]	Baking [min]	Thickn. [nm]
1. layer	P(MMA-MAA) [1]EL9	4000	1	$\sim$ 350
2. layer	PMMA [2]A4	4000	1	$\sim$ 200
absorber	PMMA [3]A11	1000	5	$\sim$ 5000

3.3.4 E-beam Patterning

The exposure was done with either LEO 1430 SEM (single pixels) or Raith e-LiNE (arrays). Because the smallest features of the TES are in the order of µm the resolution of the LEO was sufficient. But LEO does not have good enough control of the movement of the stage, so the e-LiNE was used in the making of the arrays.

With LEO the parameters for the exposure were: Acceleration voltage 30 kV, beam current about 4 nA, spotsize about 600-700, resist sensitivity 150 µC/cm^2 and step size 5 px. With e-LiNE the following parameters were used: Acceleration voltage 20 kV, aperture 120 µm, current $\sim$ 6 nA, area dose 200 µAs/cm^2 and stepsize 38 pixels.

3.3.5 Development and Plasma Cleaning

After the exposure the samples were developed. First they were developed with MIBK/isopropanole solution (1:2), which develops the resist vertically. The samples were immersed in the solution for 45 s, after which they were washed with isopropanol and blow dried with N_2. Next they were developed with methoxyethanol/methanol solution (1:2), that is more selective to the copolymer resist. This will produce a undercut profile (Fig. 3.4) that will help the lift-off process. The samples were developed this time only for 6 s and then again washed and dried.

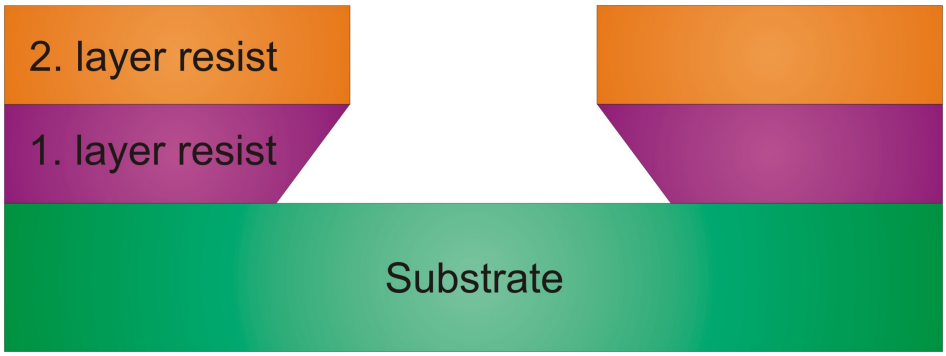

Figure 3.4: Schematical figure the undercut profile in the two layer resist.

[1]EL9 = solvent ethyl lactate, 9 mass procent of resist
[2]A4 = solvent anisole, 4 mass procent of resist
[3]A11 = solvent anisole, 11 mass procent of resist

When the samples were developed, they were next cleaned from organic dirt and resist residues in Reactive Ion Etcher (RIE). The samples were cleaned in Oxford Instruments Plasmalab80Plus RIE for 30 s in 50 sccm oxygen flow in 40 mTorr pressure at 30 °C temperature and 60 W power.

3.3.6 Evaporation of Materials and Lift-off

The next step in lithography process is the deposition of materials. The evaporation of metals was done in ultra high vacuum (UHV) electron beam evaporator, which has a pressure of 10^{-8} mbar in the vacuum chamber. The evaporation of insulator material Al_2O_3 and absorber material bismuth was done in Balzers BAE 250T HV (high vacuum) electron beam evaporator, which has a pressure of 10^{-5} mbar in the vacuum chamber. In table 3.2 are evaporation parameters for a CorTESs and in table 3.3 are evaporation parameters for a TES array. Notice that no absorbers were deposited with the CorTESs.

After the deposition the lift-off for the samples were done in hot acetone and the samples were again washed and dried. With some materials the sample were left over night in the acetone to guarantee a good lift-off. After the lift-off step the next process round was done unless it was the last step.

Table 3.2: Evaporation parameters for a CorTES

Round	Material	Thickn. [nm]	Speed [nm/s]	Angle [°]
1	Nb	40.0	0.1	0
	Au	10.0	0.1	0
2	Ti	5.0	0.1	0
	Au	45.0	0.1	0
	Ti	40.6	0.1	0
	Au	10.0	0.1	0
[4]3	Al_2O_3	121.0	0.12	8
4	Ti	10.0	0.1	0
	Ti	5.0	0.1	10
	Ti	5.0	0.1	[5]-10
	Ti	10.0	0.1	10
	Ti	10.0	0.1	-10
	Nb	10.0	0.1	0
	Nb	5.0	0.1	10
	Nb	5.0	0.1	-10

Table 3.3: Evaporation parameters for a TES array

Round	Material	Thickn. [nm]	Speed [nm/s]	Angle [°]
1	Ti	5.0	0.1	0
	Au	50.0	0.1	0
	Ti	40.0	0.1	0
	Au	10.0	0.1	0
2	Nb	10.0	0.1	0
	Nb	10.0	0.1	10
	Nb	10.0	0.1	-10
	Nb	5.0	0.1	10
	Nb	5.0	0.1	-10
[6]3	Bi	500	2.0	0
	Cu	200	1.0	0
	Bi	2000	2.0	0
	Cu	200	1.0	0

[4]Rotating stage
[5]90° rotation of stage
[6]Rotating stage

3.4 TES Measurements

As the operation point of TESs is around 100 mK sophisticated cooling of the samples is needed. Measurements were done in a dilution refrigerator, which utilizises special properties of ^{3}He-^{4}He-mixtures in the cooldown process.

First the sample was attached to a sample carrier with varnish, and the aluminum bonds for measurement lines were made with F&K Delvotec 5432 ultrasonic wedge wire bonder. Next the sample carrier was mounted on the measurement cryostat. Next a vacuum can was attached to the cryostat and it was precooled with liquid nitrogen (LN_2) to 77 K after which it was cooled to 4.2 K with liquid helium (LHe). After this it was cooled down to base temperature of about 50 mK, where measurements were made. The operation of a dilution refrigator in discussed next.

^{3}He-^{4}He dilution refrigerator works on the basis of phase separation between ^{3}He and ^{4}He [47]. Below temperatures of 0.87 K the two phases separate spontaneously to a normal fluid phase rich in ^{3}He on top of a superfluid phase rich in ^{4}He. A controlled cycle of mixing, diffusion, and condensing can be used to achieve cooling well above the 4.2 K surrounding bath temperature of liquid helium.

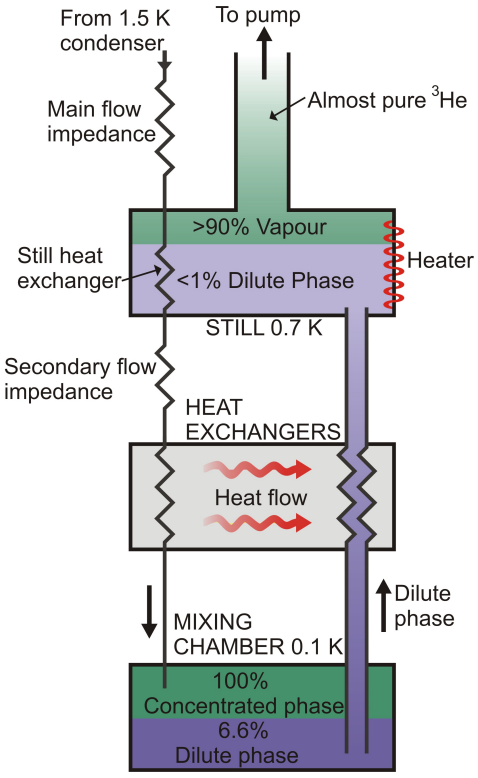

Figure 3.5: Schematical image of a dilution refrigerator. When ^{3}He atoms are pumped away from the dilute phase ^{3}He atoms enter the dilute phase from the concentrated phase through a phase boundary, which requires energy. This energy is taken from the surroundings, which effectively cools down the mixing chamber.

The basic structure of a dilution refrigerator is shown in Fig. 3.5. ^{3}He gas coming from room temperature is precooled by the 4.2 K ^{4}He bath. It is then condensed at about 1.5 K in a second ^{4}He bath called the pot. Below this ^{4}He refrigerator, a main flow impedance is needed to establish sufficient pressure for the incoming ^{3}He gas to condense. Next the ^{3}He gas will flow through heat exchangers that is in thermal contact with the still at 0.7 K. Below the still there is a secondary impedance to prevent re-evaporation of ^{3}He. Next, after flowing through heat exchangers to precool the ^{3}He gas it enters the upper, concentrated phase in the mixing chamber. A wider tube for the dilute phase in the refrigerator leaves the lower dilute mixture phase of the mixing chamber, and through the heat exchanger to precool the incoming ^{3}He. Then it enters the dilute liquid phase in the still. Vapour above the liquid phase in the still has concentration of about 90 % of ^{3}He. Now if the still is pumped and the condensation line is resupplied continuously with ^{3}He gas a closed ^{3}He circuit is formed where ^{3}He is forced down the condensation line. Then again after liquefaction and precooling it enters the concentrated phase in the mixing chamber. It will cross the phase boundary and by doing so it will cool down the system. After this it will leave the mixing chamber and be pushed to still where it will evaporate. Circulation of the system is achieved by pumping the system at room temperature. This cycle is done continuosly to achieve temperatures less than 100 mK easily.

Most of the measurements in this temperature range were done with home built PDR50 dilution refrigerators, which have a base temperature of 50 mK. Measurements of the array TES were done in Kelvinox MX400, which can go as low as 7 mK. The low base temperature of the Kelvinox system was not the motivation for its use but the greater amount of measurement lines needed in the array measurements that the home built PDR lacked.

The sample stage has a RuO temperature sensor integrated to it and the resistance was measured with AVS resistance bridge. In the critical temperature measurements the resistance of TESs were measured with current biased 4-probe method with a lock-in amplifier, as shown in Fig. 3.6.

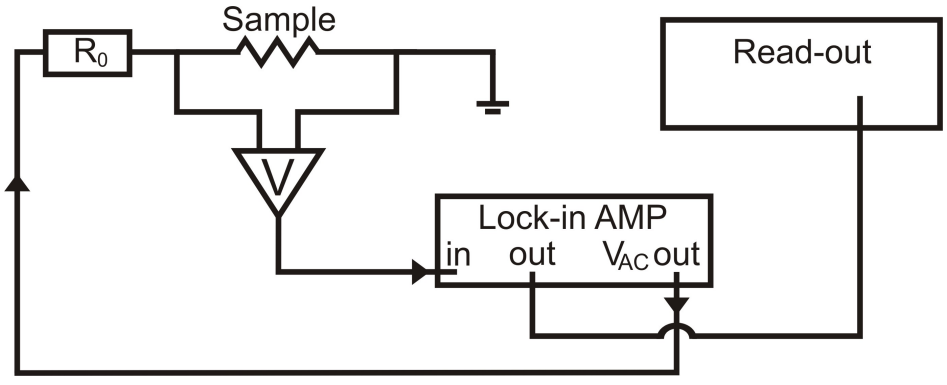

Figure 3.6: Schematics of T_c measurement setup.

Also a measurement was done with radioactive ^{55}Fe as an X-ray source. The detector used was a single pixel from a TES array. The purpose of this was just to demonstrate that the TESs actually work, although the deposition of the absorber had pretty much destroyed the sensitivity of the TES because it was done in a simplified way. The read-out of the pulses was done with electronic circuit consisting of two stage SQUID device (Fig. 3.7). The change in resistance of the TES film changes the current through the film that creates magnetic field, which can be measured very accurately with the SQUID system. Schematic of the SQUID stage in Fig. 3.7.

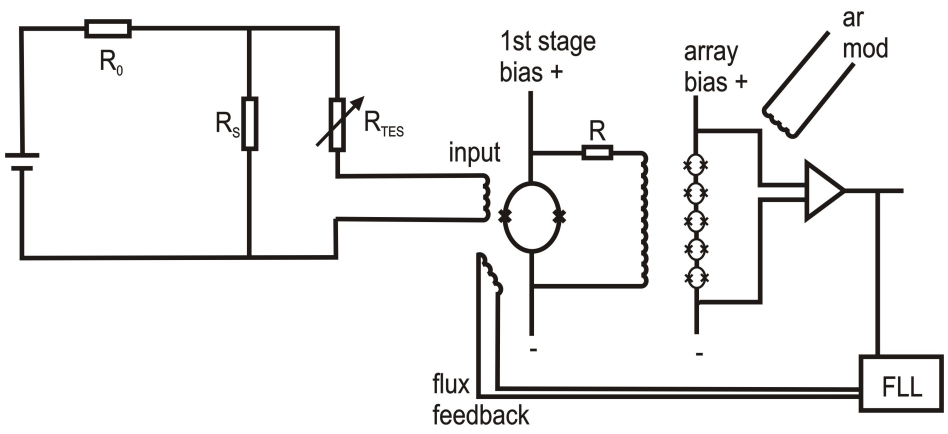

Figure 3.7: Schematics of a single pixel TES readout. TES is constant voltage biased, Rs << Rtes. Current change caused by heating from absorbing a photon is read out by the SQUID, which is operated in flux locked loop mode. In multiplexed operation one SQUID measures several pixels. Figure from K. Kinnunen.

The SQUID is used as current amplifier with flux locked loop (FLL) that locks the operating point of the SQUID, which linearises the gain with a separate flux feedback coil. The feedback coil keeps the magnetic flux through the SQUID constant and the measured signal is the feedback current. The second stage SQUID array is used as a preamplification of the SQUID signal and to match the impedance of the SQUID amplifier with the electronics at the room temperature [48].

3.5 TES Results

3.5.1 Single Pixel Results

To be able to produce consistent critical temperatures of the superconducting layer one needs to know well the ratio between the superconducting Ti and the normal metal Au. No clear regression was found but a ratio between 1.2–1.35 seemed to produce a T_c of $\sim$ 100 mK, which is desired (Fig. 3.8). The thickness of titanium was always kept constant at 35 nm. It was noticed that the ratio is very sensitive to contamination of UHV and other external factors. For example if the gold in the evaporator was almost finished this would affect the critical temperature.

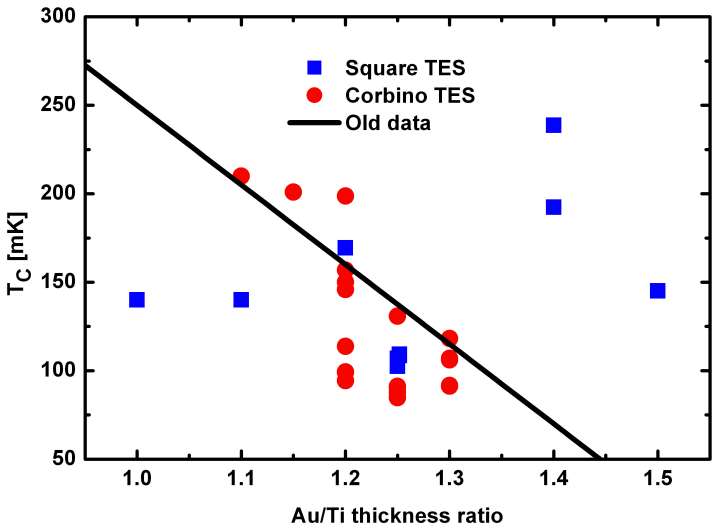

Figure 3.8: Gold/Titanium ratios versus critical temperatures. Thickness of titanium kept constant (35 nm). Old data linear fit from [49].

The normal state resistance R_N is also a very important parameter. The square TESs that had T_c near 100 mK usually had the R_N around 400 mΩ – 600 mΩ. The CorTESs instead had it in the range of 100 mΩ – 200 mΩ, but due to the Corbino disk geometry the R_N can be lowered by increasing the size of the center contact, since

$$R_N = A \ln \frac{r_o}{r_i}, \tag{3.1}$$

where r_i is the radius of the inner contact, r_o of the outer one and A is a parameter that includes resistivity and thickness of the sample. This was tested and the data is in Fig. 3.9. The samples were not fabricated at the same time, although they were fabricated with same parameters (e.g. film thickness), so the T_c:s are not the same.

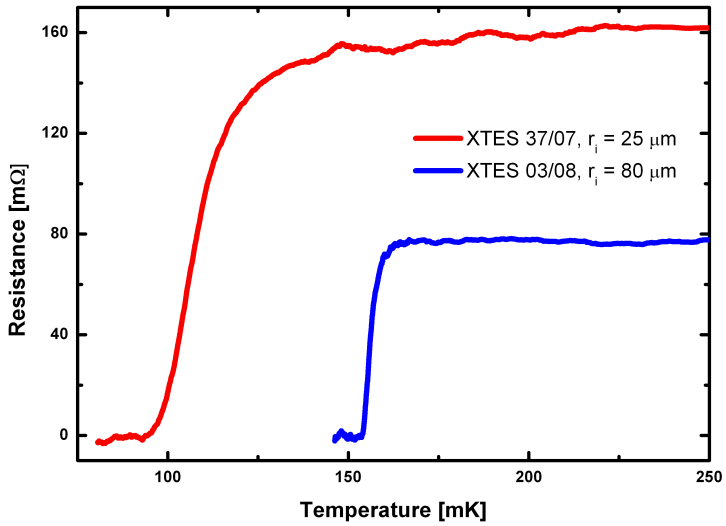

Figure 3.9: Transitions of two CorTESs with different inner radiuses.

The XTES 37/07 had a $r_i = 25$ μm, r_o=150 μm (same with all CorTESs) and $R_N =$ 162 mΩ. From this it can be calculated with eq. (3.1) that

$$A = 90.41 \text{ m}\Omega. \tag{3.2}$$

The XTES 03/08 had an inner radius of 80 μm and if we assume that the A is the same as with the XTES 07/08 then the equation (3.1) gives that $R_N = 56.83$ mΩ, when the measured value was 77.33 mΩ. The difference between the measured and the calculated value may be due to the fact that the equation (3.1) is valid for an OTES and some error comes when used with XTES due to slicing of the TES film. The difference in the T_c:s is quite large ($\sim$ 50 mK), which suggests that there was some contamination in the UHV chamber, while depositing the XTES 37/07. Still, the R_N of the XTES 03/08 has dropped, which was the aimed result.

Although the TES is shielded from external magnetic field by the upper superconducting niobium bias contact, a hole is needed in the top bias contact to couple the absorber to the TES. These kind of TESs with a hole in the top bias were fabricated and the effect of the magnetic field was studied. It was noticed that the magnetic field had some effect for example on the R(T)– and IV–characteristics but more resesarch is needed. The magnetic field effects may arise because the field can penetrate through the hole in the top bias and magnetic flux may be trapped inside the TES, which in turn effects the performance of the TES.

3.5.2 TES Array Results

The first TES array made in Nanoscience Center was made easily with the equipment in the facility. The first manufactured one was 32-pixel square TES array (Fig 3.10). Although a proper UV-lithography device could be a better choice for line widths used in TESs, e-beam lithography can be used as long as there isn't any industrial scale manufacturing of the detectors. With the UV-lithography system in NSC it is very hard or even impossible to align different processing layers with each other.

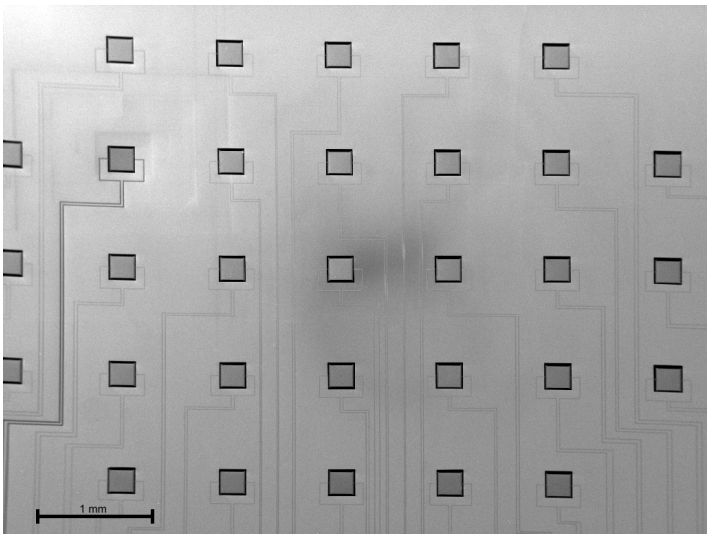

Figure 3.10: First 32 pixel TES array made in Jyväskylä.

As the TESs are biased in the narrow transition, the T_c has to be uniform across the whole TES array meaning that all the pixels should have the same critical temperature. Many T_c:s were measured, and it was observed that there was some deviation in the values as can be seen in Fig. 3.11. The deviation has to be made smaller in order to maximize the performance of a TES array. The only way to make this happen is to make the fabrication process somehow cleaner, which means that the deposition of the Au/Ti -layer should contain no contamination and the metals should not contaminate after the deposition.

Absorber material was evaporated on TES array 02/08 (2.5 μm Bi + 0.4 μm Cu). It was deposited to cover all of the actual superconducting film, which is probably not the best way to do it because it pretty much destroys the sensitivity of the superconducting transition as can be seen in Fig. 3.12 (probably copper somehow affects the TES film). This was done just to test the evaporation of the bismuth and accuracy of the e-beam lithography process. Different absorber structures have been made e.g. one working idea is a mushroom like structure demonstrated by NASA [50].

The demonstration of the pulses from the X-ray experiment is shown in Fig. 3.13. Because the source was not collimated in any way one can see that there is pile up of

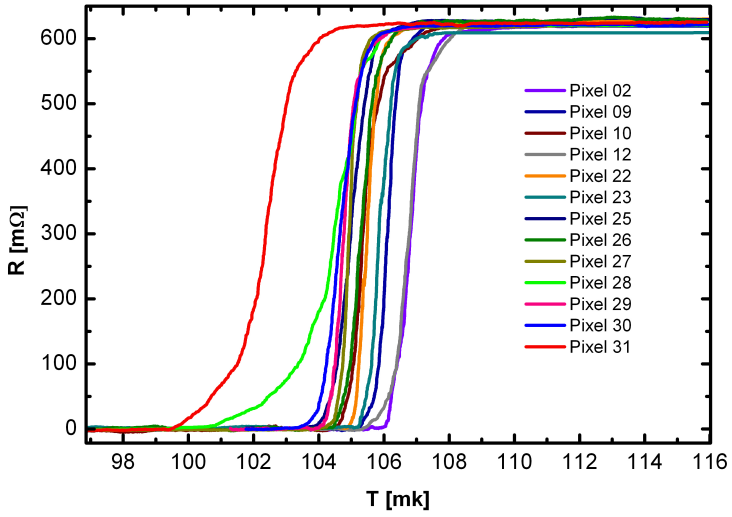

Figure 3.11: Critical temperatures of TES array 02/08 pixels.

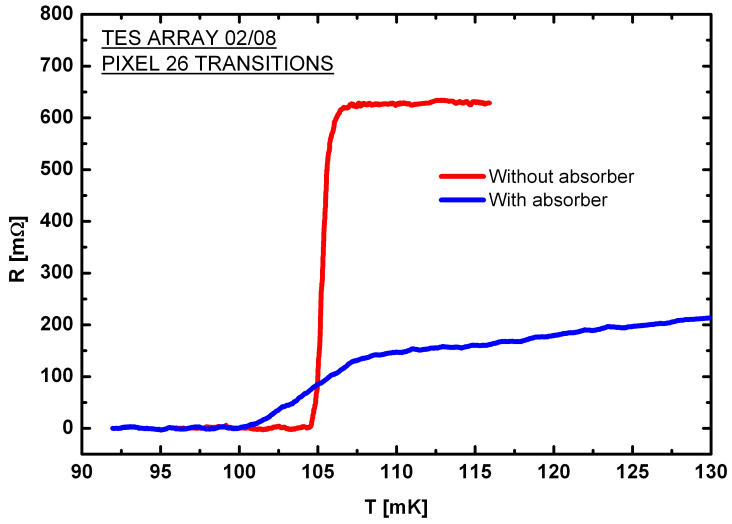

Figure 3.12: Transition of a pixel from TES array before and after deposition of absorber.

the pulses due to heavy bombardment of the TES by X-rays.

In Fig. 3.14 is a single pulse of the SQUID output as a function of time. The pulse time is a bit long ($\sim$ few ms) but it will be reduced dramatically after fine tuning of the fabrication process. With same materials used in TES film and same X-ray source a group in Japan has demonstrated a pulse times of 15 μs [51] and the theoretical limits

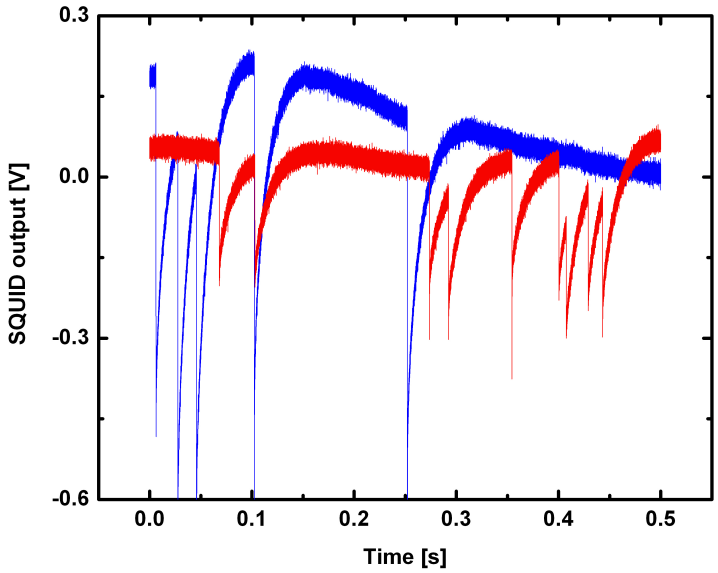

Figure 3.13: X-ray induced pulses with two different bias points. The blue line is lower in the transition and the red one higher. Slope in the base line is due to drift in the bath temperature.

are in the order of μs [52].

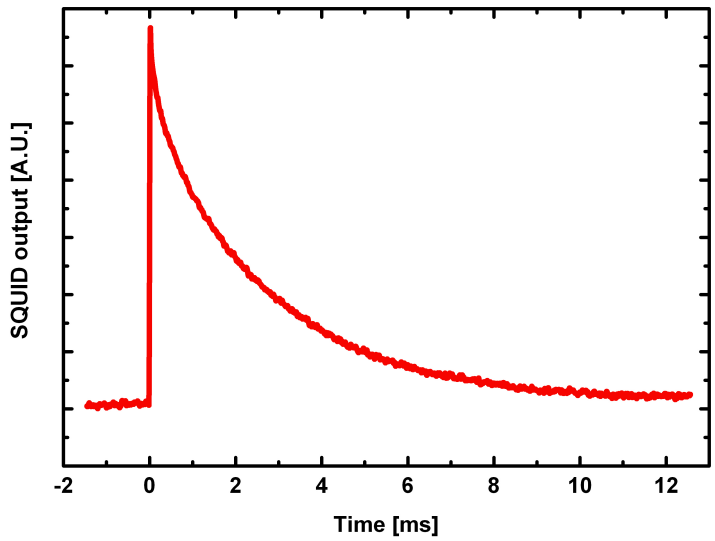

Figure 3.14: Single X-ray induced pulse. $\tau = 1.54$ ms.

Chapter 4

Absorber Development

4.1 Bismuth Samples

To study the resistivity of bismuth and the effect of annealing bismuth samples were fabricated using the same kind of lithography steps as discussed in the fabrication of TESs. The bismuth samples were simply a strip of bismuth and bonding pads on a 300 nm thick Si_3N_4 on 300 µm silicon. In some of the strips there was a 5 nm – 45 nm gold layer beneath the 2 µm Bi strip that was 1.34 mm long and 50 µm wide (Fig. 4.1). Bismuth was evaporated with Balzers with speeds in the range of 1–2 nm/s and the gold with UHV at 0.1 nm/s.

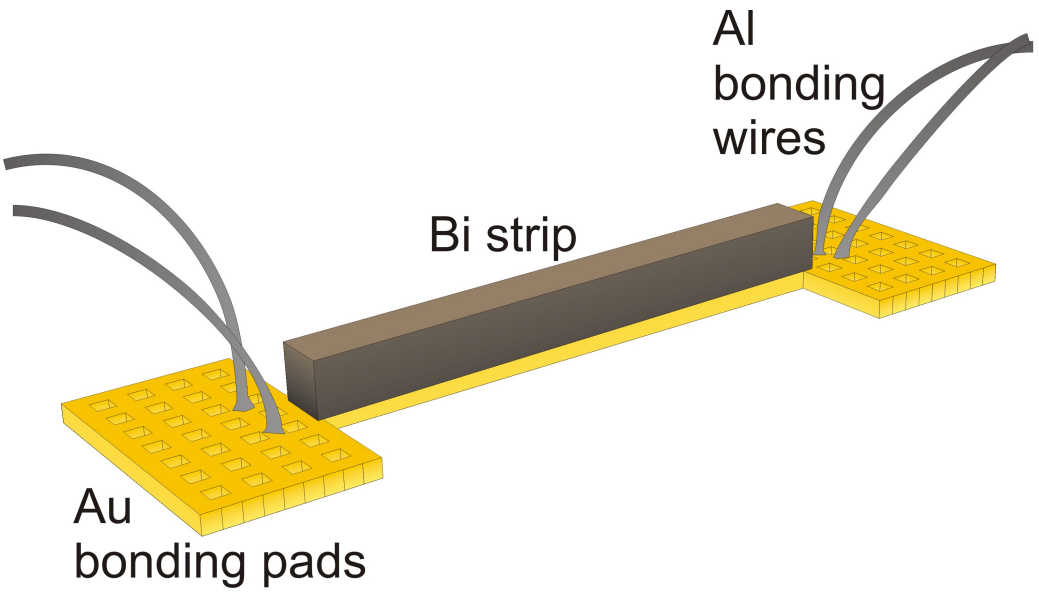

Figure 4.1: Schematical image of bismuth strip and golden bonding pads with aluminium bonding wires.

Also plain gold strips were fabricated as well plain bismuth strips to study their resistivities separately.

4.2 Bismuth Resistivity Measurements

The resistance of bismuth was measured as a function of temperature from room temperature to liquid helium temperature.

First the sample was attached to the sample carrier as discussed with the TES measurements. Next the sample carrier was mounted on the measurement dipstick, which had a thermometer integrated to it. The temperature sensor used was a Cernox thin film resistance cryogenic temperature sensor made by Lakeshore. The dipstick was open structure so it didn't have any vacuum or other kind of shielding.

The dipstick was first slowly dipped in to LN_2 while the resistance of the sample was being measured as well as the resistance of the thermometer. Both the sample and the thermometer were measured in 4-probe measurement with AVS resistance bridges. Sometimes the resistance of the sample was measured with a lock-in amplifier. After the sample was cooled down to 77 K, the dip stick was moved into LHe dewar and then it was slowly lowered to the level of the LHe, where it was cooled down to 4.2 K. Then the sample was lifted up and let to warm up while its resistance was being measured.

4.3 Bismuth Results

Because bismuth is used as an absorber material its properties need to be well known. One figure of merit for a material is the temperature dependency of its resistivity. This was measured from room temperature down to 4 K and even down to 50 mK with some samples.

Because the bismuth layer was deposited by evaporation the structure was polycrystalline (see Fig. 4.2). After the deposition, annealing was performed to make absorber as close to single crystal structure as possible. This would increase the electrical conductivity and thus the thermal conductivity, which is needed in a good absorber.

Bismuth was evaporated with different deposition speeds from 1 nm/s to 3 nm/s and much correlation was not found with the crystal structure and the deposition speed contrary to previous observation in JYU [53], although more defects like visible holes would occur in the bismuth layer when depositing with greater speeds. The thickness of the Bi layers varied from 2 μm – 3μm.

The annealing was done at about 260 °C - 265 °C in vacuum ($< 10^{-4}$ mbar) for c. 5 hours. The melting point of Bi is 271 °C. A thin layer of gold (7 nm) was also deposited before the bismuth layer in order to help the formation of better crystal structure [54]. It was observed that if no gold was under the bismuth there was no visible change in the crystal structure, atleast not at the surface, compared to the dramatic change when gold was used as can be seen in figure 4.2. The polycrystalline structure was transformed towards more single crystal -like structure with no clear individual domains after the annealing.

One problem that was encountered was that during annealing, bismuth somehow

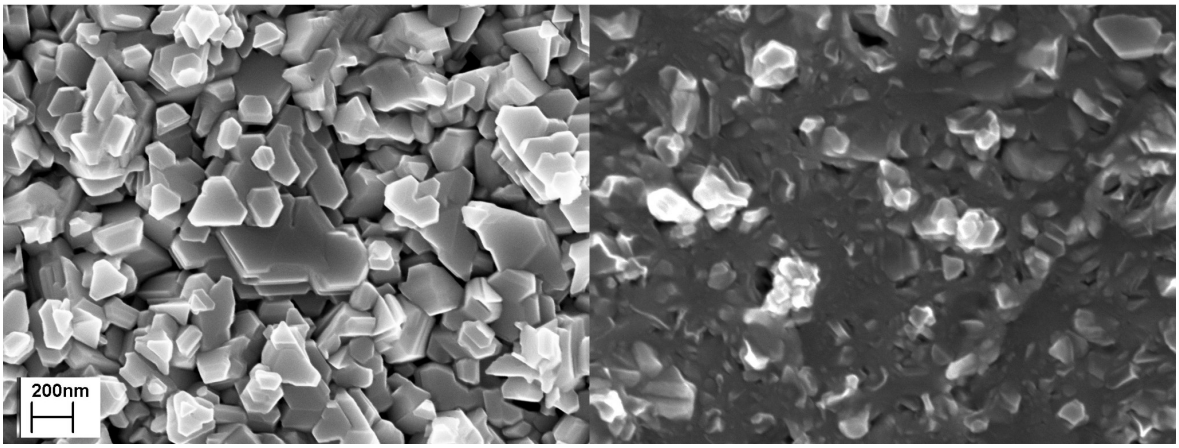

Figure 4.2: Left: Surface of the bismuth strip before annealing. Right: Surface of the bismuth strip after annealing. A thin layer of gold (5 nm) was used under the bismuth.

sucks in the surrounding gold that it is in contact with as can be seen in Fig. 4.3. Obviously this is a problem because there is gold in the actual TES layer of the detector. The effect was seen even if the bismuth strip was not annealed in high temperatures but just storaged at room temperature for six months or so.

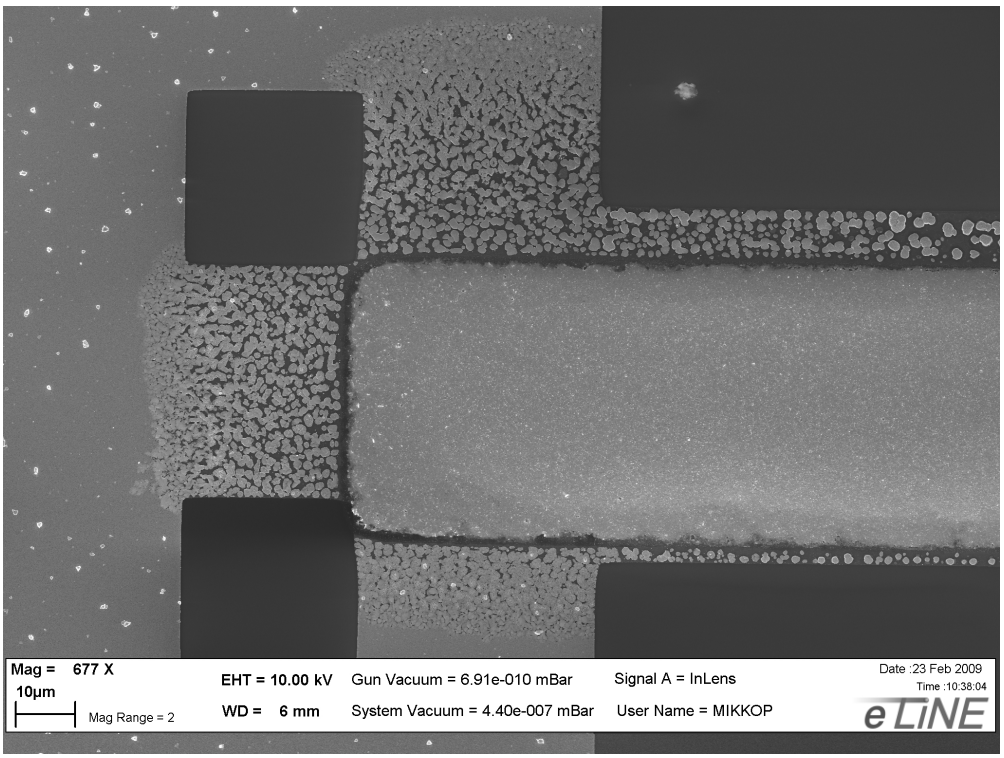

Figure 4.3: The bismuth strip has somehow sucked the gold out of bonding pads during annealing.

The resistivity of bismuth was dramatically lower after annealing, which can be seen in figure 4.4. The RRR (residual resistivity ratio) value (0.52) didn't change due to annealing.

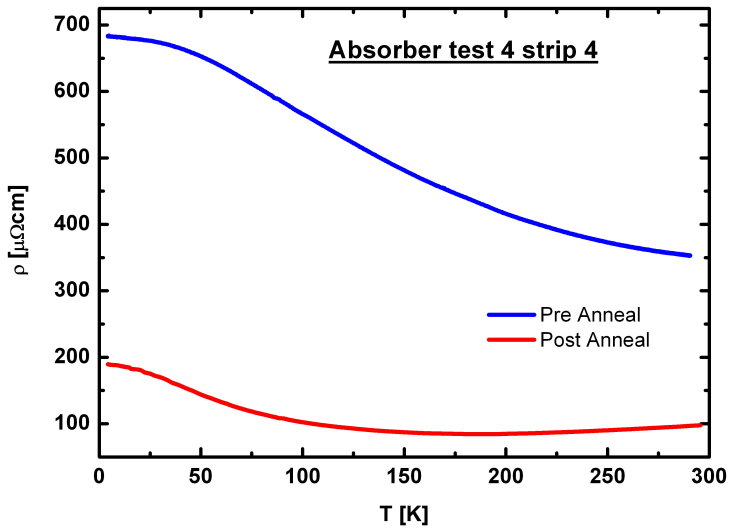

Figure 4.4: Resistivity of the bismuth strip before and after annealing (5 nm layer of Au under Bi).

Resistances of individual gold and bismuth strips as well as bismuth on top of gold were measured just to see how much of the conductivity comes from gold and how much from bismuth. The thickness of the gold layer was 45 nm and bismuth was 2 μm thick. In the analysis the resistances of Au and Bi were added in parallel and they were compared with the actual Au/Bi strip. This revealed that there is some kind of extra resistance that arises from the surface contact of the two different material. Data of this is in Fig. 4.5.

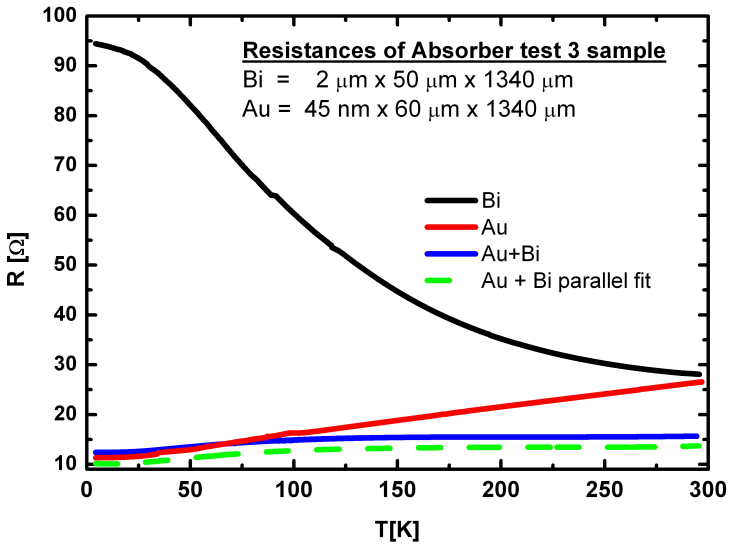

Figure 4.5: Resistances of Au, Bi and Au+Bi strips as well as calculated parallel fit of Au and Bi strips.

Although the actual height of the bismuth strip was not that important in these measurements in the future we have to be able to be control it accurately to get the desired heat capacity C and thermal conductance G. Furhermore the thickness of the absorber determines the energy range where photons are absorbed efficiently.

The thickness of the strip was measured with atomic force microscope (AFM) and this was compared to the expected value. It was found that there were quite huge errors in the readings of evaporators thickness monitor. Also it was noticed that evaporation speeds played some kind of role in these errors. Data of this is in Fig. 4.6 and Fig. 4.7.

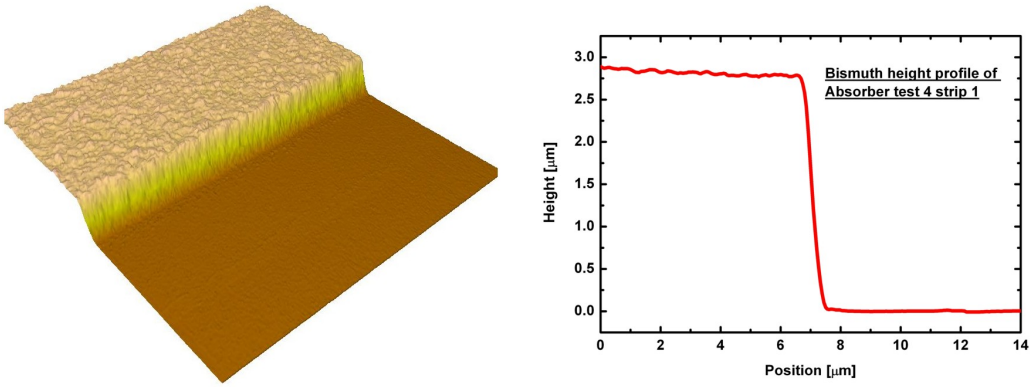

Figure 4.6: Height profile of bismuth strip. The height of the strip was about 2.8 μm when it was supposed to be 2.0 μm. Evaporation speed was less than 1 nm/s.

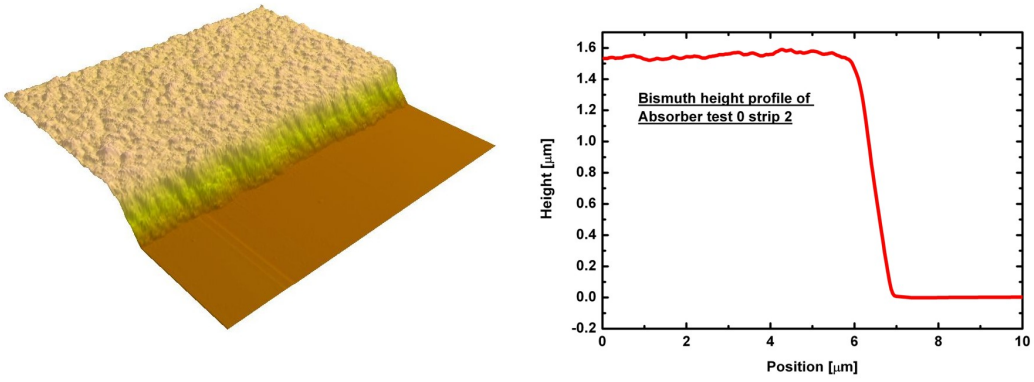

Figure 4.7: Height profile of another bismuth strip. The height of the strip was about 1.5 μm when it was supposed to be 2.0 μm. Evaporation speed was more than 2 nm/s.

Chapter 5

ALD Tests

5.1 ALD Test Samples

A test to use atomic layer deposition (ALD) deposited insulating layer in the CorTESs was also done. ALD method is a thin film deposition technique that is based on the sequential use of a gas phase chemical process and it can be controlled with atomic layer accuracy. This should result in very uniform pinhole free thin films.

We collaborated with University of Lappeenranta who have the expertise in the ALD deposition techniques. They fabricated Al_2O_3 thin films with the ALD method on our samples. The conventional way of evaporating the Al_2O_3 thin films has couple of drawbacks, which is why we wanted to test the ALD method. First of all, the film thickness needs to be over 100 nm thick to ensure that there is no pinholes. The height is rather large, when a 30 nm Nb thin film has to climb over this wall and it might cause the Nb film to crack from the kink. Also the ALD deposited thin film does not have any impurities in it unlike the e-beam evaporated films have, so the ALD deposited thin films do not bring any contamination to the samples.

The first sample was a lift-off test, where circular patterns were patterned on resist with e-beam lithography. Doughnut shapes with outer radius of 300 µm with different inner radiuses were made. The resist used was the same 2-layer resist as used in fabrication of TESs.

The second type of samples were plain metal strips (Au and Nb) on top of which the Al_2O_3 was to be deposited with the ALD. The strips were about 1 mm × 300 µm in size. Later a layer of the same metal was deposited on top of the Al_2O_3. Afterwards we could measure if there was current flowing through the Al_2O_3, which would mean that there are pinholes in the ALD deposited insulator layer.

Also, square TESs were made and Al_2O_3 were deposited on top of them to see if the ALD process itself had some effect in the properties of the TESs. Reference TESs were made at the same time with the ones that got the Al_2O_3-layer on top of them.

5.2 ALD Test Measurements

The ALD sample was mounted on the sample carrier and bonded as discussed above. Then the sample was mounted on the so-called 1-K cryostat and a vacuum can was sealed with a indium O-ring. The cryostat also had a thermoelement, whose resistance was measured with AVS resistance bridge.

Next the vacuum can was pumped to a vacuum and then the cryostat was lowered in LN_2 and small amount of air was let inside the vacuum can as a heat exchange gas. The inside of the vacuum can was let to cool down to 77 K, which took about 45 min. Then the cryostat was lowered into LHe dewar and let to cool down near 4 K. Then the pumping of a so–called pot would be started.

In the pot a small fraction of the LHe from the main bath flows through a flow impedance into vessel located in vacuum can inside the cryostat. Then the vessel is pumped and the LHe is evaporated. The liquid from the main bath is isenthalpically expanded through the impedance and will arrive at lower temperature in the evaporation vessel [55]. This vessel fills up until the level of the liquid in the pumping tube is at height where the heat transferred from the main helium bath through this column of liquid and the heat from the experiment balance the cooling power of the refrigerator available from the latent heat of evaporation. With this method we could reach a base temperature of 1.6 K.

The purpose of this measurement was to determine if a current would flow between the two Nb-layers separated by a thin (3nm) Al_2O_3-layer deposited with ALD. The resistance of the sample was measured from room temperature to the base temperature of the cryostat with a lock-in amplifier. At the base temperature a conductance measurement was done with a homemade voltage sweepbox, current amplifier, voltage amplifier and a lock-in amplifier. The measurement setup is shown in Fig. 5.1.

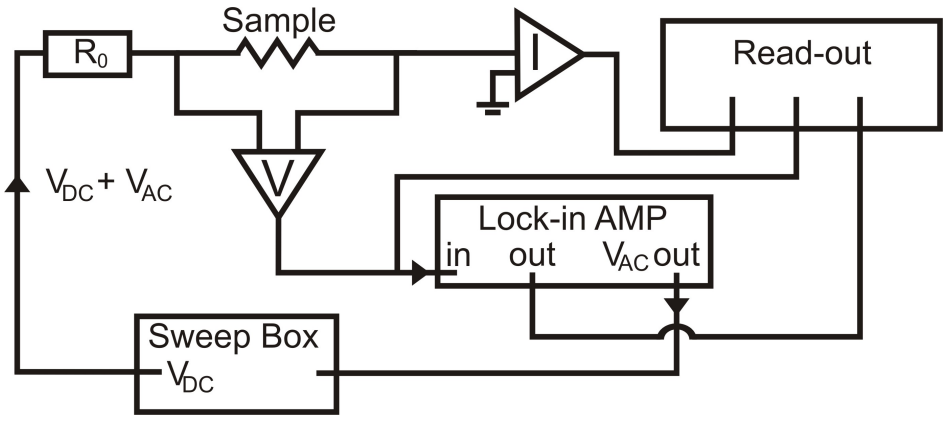

Figure 5.1: Measurement setup of the conductance and IV measurement.

The sample was current biased with 1 MΩ resistor R_0 and DC voltage. The input voltage (± 5 V) was generated by the voltage sweep box with a low frequency (17 Hz)

AC signal summed to it from the lock-in amplifier. The voltage over the sample was amplified and fed to the lock-in amplifier, which picked up the AC components and so the differential resistance $\frac{\mathrm{d}\,V}{\mathrm{d}\,I}$ could be measured. Also the amplified current and voltage were recorded with measurement software to get the IV-characteristics.

5.3 ALD Test Results

Since the Al_2O_3 will act solely as an insulating layer the current flow should be zero between the two Nb layers. It was soon discovered that this was not the case. The 3 nm layer of insulating material is simply too thin for such large areas. When consulting with Lappeenranta University of Technology we asked for a 10 nm layer, which requires about 100 processing cycles but instead they made only 30 cycles ($\sim$ 3 nm). From

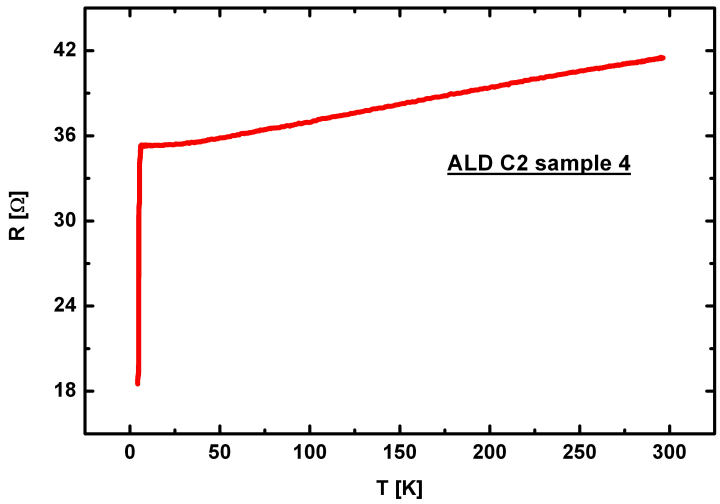

Figure 5.2: Resistance of Nb-AlOx-Nb sample. The increase of resistance as a function of temperature indicates that the junction is not a tunneling junction. Measured from 4.2 K to room temperature.

Fig. (5.2) it can be seen that there is some kind of transition at $\sim$ 5 K but the sample does not go completely into superconducting state because there is some residual resistivity after the transition. Also, if the interaction between the Nb-layers would be a tunnel junction the resistance would increase when going to smaller temperatures, which clearly is not the case here.

From the lift-off test we can conclude that the double layer resist was not good for this purpose and it was too thick. Because ALD covers every surface i.e. step coverage is fully conformal, the undercut profile may result in even worse lift-off than without the under–cut [46]. From Fig (5.3) it can be seen that the lift-off process didn't succeed

completely, especially inside of the ring structure, which is the most crucial point in the future if ALD is used in actual TES detectors. So, further experiments are still needed with ALD. A single layer resist less than 100 nm thick could achieve better results.

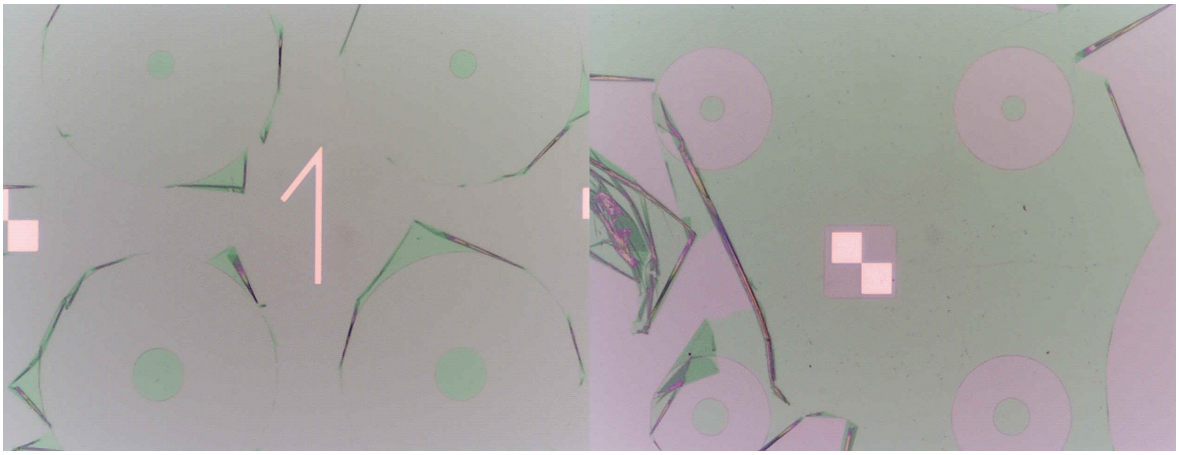

Figure 5.3: ALD samples after lift-off. Shreds of AlOx can be seen.

From conductance measurements we found that in the IV–characteristics there were step-like behavior at certain voltages (currents). These can be seen in Fig 5.4 as well as the peaks in the differential resistance $\mathrm{d}V/\mathrm{d}I$. These peaks in the differential resistance may result from superconducting point contacts [56] due to pinholes in the Al_2O_3 thin film.

When the ALD deposited Al_2O_3 tests were done we also wanted to see the effect of the ALD processing on the T_c of the TESs. For this a reference sample and another sample were fabricated, which were done identically. The other sample then went through the ALD processing where the Al_2O_3 layer was deposited on top of the TES layer. After this we measured the T_c:s of both of the samples.

From Fig 5.5 one can see that the processing of the ALD has some effect on the critical temperature. This is probably from the fact that the processing was done at 95 °C, which somehow anneals the metal layers and moves the transition to higher temperature, although it has been previously seen that baking of the TESs decreases the T_c. The displacement is not too great and as long as it is consistent it should not be a serious problem. One can also see that after the ALD processing the steepness of the transition (α) has changed slightly.

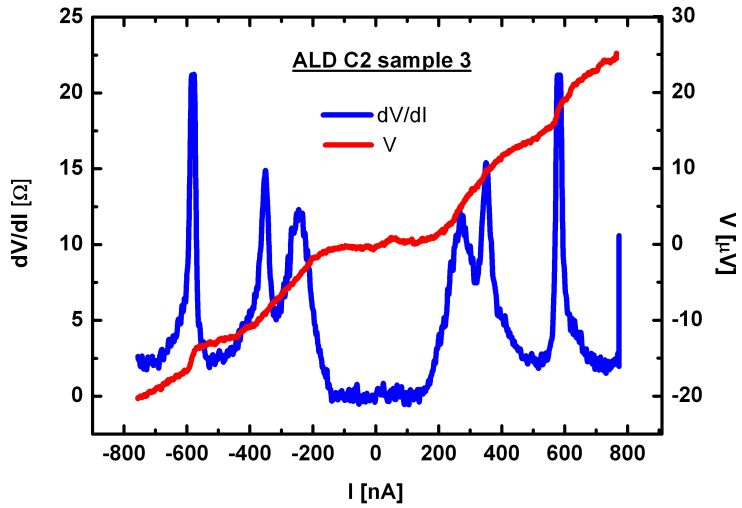

Figure 5.4: Steplike IV characteristics as well as peaks in differential resistance. T = 1.6 K.

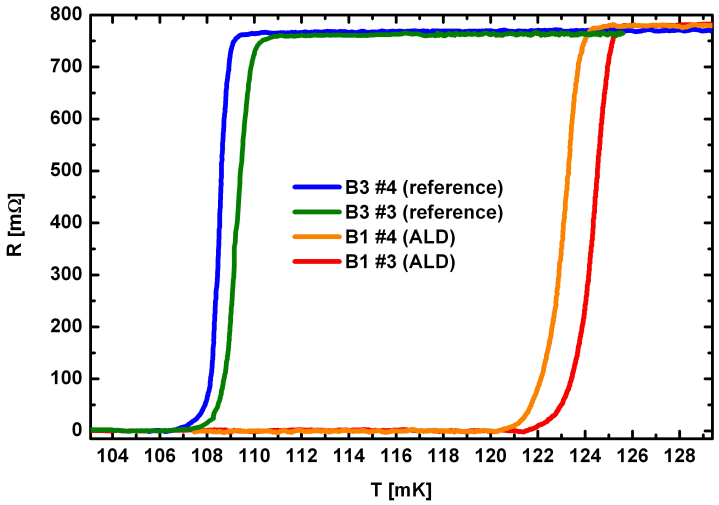

Figure 5.5: Critical temperatures of two reference TESs and a two TESs after ALD procession.

Chapter 6

Conclusions

The first and maybe most important conclusion of this thesis is that a TES array can be manufactured in NSC in Jyväskylä. TES pixels in the array had some deviation in the critical temperatures. All the T_c:s were in the range of 102 mK – 107 mK, when maybe a deviation of 1 mK could be acceptable. If the T_c:s are not consistent, it will cause them not to be in the same operation point when biased. This will then lead to a case, where the single pixels respond differently to same energy photons, which of course is not desirable. In the future this problem will have to be somehow overcome. One possibility would be to cover the backside of the array with some material with good thermal conductance (e.g. aluminium) to ensure that there are no temperature gradients in the substrate during evaporation. Such gradients can have an effect on the T_c:s. Afterwards, this thermalization layer could be etched away.

It can be concluded, that with the UHV evaporator it is difficult to get the same critical temperatures with every evaporation of the superconducting thin film. The materials in the chamber should always be extremely pure and the ambient atmosphere always exactly the same for this to be achieved. On the other hand, it does not really matter if the T_c:s of an array are 100 mK or 110 mK as long as they are consistent with every pixel of the array.

If we will decide to use CorTES geometry in the TES arrays with the ALD deposited insulating layer, the ALD process itself does not seem to be a problem. It changes the T_c just slightly. But now we only had a Al_2O_3 layer of 3 nm, which requires about 30 cycles with the ALD machine. The desired thickness would be in the range of 10 nm – 20 nm, that would require $\sim 100 - 200$ cycles and because it is done at reasonably high temperatures (~ 100 °C) this process could affect the T_c more. For example, it might anneal the titanium–gold layer, rearranging the crystal structure and thus changing the T_c. Furthermore the thin film of 3 nm is clearly too thin and a thicker layer should avoid apparent pinholes. The resist used for the Al_2O_3 deposition probably has to be thinner because it didn't lift-off properly with thicker one. Also one layer resist could be more convinient with the ALD method instead of two, because an undercut profile may just make the lift-off harder than without it.

The properties of bismuth are rather tricky. When deposited with electron beam evaporator, it forms small chunks or flakes c. 200 nm in diameter instead of a uniform thin film. Annealing the layer can be used to make the layer, if not single crystal, atleast more single crystal like. Then it has more better attributes like better thermal conductance and smaller resistivity. But if the absorber is deposited last, which of course is the simplest way, the annealing process would probably destroy the TES film; if not completely, atleast change its characteristics dramatically. So the annealing of TES detector at high temperatures is really not a choice, unless the absorber is done first and then the rest of the TES detector is done after the bismuth has already been annealed. This is not a simple problem and it requires more research in the future. One solution is to change the absorbing material completely but unfortunately there aren't many materials to choose from. One option is to use plain gold as absorbing element, but this sets a upper limit for the energy of the incoming photons and also the heat capacitance of the absorbing element might become too great. To use electroplating instead of evaporating the bismuth might also be a more better way of depositing the absorber, because the crystal structure could be better.

The collaboration with the Lund University is starting to be in the point, where first actual working TES arrays will soon be tested. In initial discussion with them we have decided to make the pixel count to be 256. This should not be a problem since the first array made in NSC succeeded easily. The biggest task is probably to get the absorbing element in such a manner that the time constant of the device is more in the microsecond range ($\sim 400\mu s$) instead of milliseconds, whilst keeping the quantum efficiency high enough. One problem with the read-out technology is the reasonably high normal state resistance R_N of our TESs. We should make the R_N to be less than ~ 100 mΩ to make them work perfectly. The increasement of the inner radius of CorTESs as well as making the actual TES film thicker could be a solution.

We have ordered a state of the art adiabatic demagnetization refrigerator (ADR) that doesn't require any crygenic liquids. This machinery, together with the X-ray source in Lund and with read-out technology from NIST will soon form the first table-top device to do time resolved X-ray spectroscopy.

After graduating I will continue to do my doctoral thesis in this same subject and continue working with TES-projects. I'm confident that we will overcome all obstacles and will soon have a real working detectors to for example see the chemical reactions of molecules in a novel way. Also other TES-projects are already starting to rise with collaborations inside our own university.

Bibliography

[1] S. H. Moseley and J. C. Mather: *Thermal detectors as x-ray spectrometers*, J. Appl. Phys. 56, 1257 (1984)

[2] G. C. Hilton, J. M. Martinis, K. D. Irwin, N. F. Bergren, D. A. Wollman, M. E. Huber, S. Deiker, and S. W. Nam: *Microfabricated Transition-Edge X-ray Detectors*, IEEE Trans. Appl. Supercond. 11(1): 739-742; Mar (2001)

[3] K. Irwin, G. Hilton in: *Cryogenic Particle Detection*, edited by Ch. Enss, Springer-Verlag Berlin Heidelberg, (2005).

[4] D. H. Andrews, W. F. Brucksch, W. T. Ziegler, E. R. Blanchard: *Attenuated Superconductors I. For Measuring Infra-Red Radiation*, Rev. Sci. Instrum. 13, 281 (1942)

[5] K. Irwin, S. Nam, B. Cabrera, B. Chugg, G. Park, R. Welty, J. Martinis: IEEE Trans. Appl. Supercond. 5, 2690 (1995)

[6] H. K. Onnes: *The Superconductivity of Mercury* Comm. Phys. Lab. Univ. Leiden, Nos. 122 and 124, (1911).

[7] C. Kittel: *Introduction to Solid State Physics*, 7th ed., New York, John Wiley, (1996).

[8] J. G. Bednorz and K. A. Müller: *Possible high T_c superconductivity in the Ba-La-Cu-O system* Z. Physik, B 64 (1), 189-193, (1986).

[9] P. Dai, B. C. Chakoumakos, G. F. Sun, K. W. Wong, Y. Xin and D. F. Lu: *Synthesis and neutron powder diffraction study of the superconductor $HgBa_2Ca_2Cu_3O_{8+\delta}$ by Tl substitution*, Physica C: Superconductivity 243: 201-206 (1995)

[10] M. Tinkham: *Introduction to Superconductivity*, 2nd Edition, New York, McGraw-Hill, (1996).

[11] P. Monthoux D. Pines, & G. G. Lonzarich: *Superconductivity without phonons*, Nature, Vol 450j, 20/27 (2007).

[12] J. Bardeen, L. N. Cooper, and J. R. Schrieffe: *Theory of Superconductivity*, Phys. Rev. 108, 1175 (1957).

[13] S. Deiker, J. Chervenak, G. C. Hilton, K. D. Irwin, J. M. Martinis, S. Nam, D. A. Wollman: *Transition Edge Sensor Array Development,* IEEE Transactions on applied superconductivity , Vol. I 1, No. I, (2001)

[14] E. Figueroa-Felciano: *Theory and Development of Position-Sensitive Quantum Calorimeters*, Ph.D. Thesis, Stanford University, (2001).

[15] D. McCammon in: *Cryogenic Particle Detection*, edited by Ch. Enss, Springer-Verlag Berlin Heidelberg, (2005).

[16] H. F. C. Hoevers, A. C. Bento, M. P. Bruijn, L. Gottardi, M. A. N. Korevaar, W. A. Mels, and P. A. J. Korte, *Thermal fluctuation noise in a voltage biased superconducting transition edge thermometer*, Appl.Phys.Lett, 77, 26, (2000)

[17] K. D. Irwin: *Phonon-Mediated Particle Detection Using Supeconducting Tungsten Transition-Edge Sensors*, Ph.D. Thesis, Stanford University, (1995).

[18] A. Luukanen, K. M. Kinnunen, A. K. Nuottajärvi, H. F. C. Hoevers, W. M. Bergmann Tiest, and J. P. Pekola: *Fluctuation-Limited Noise in a Superconducting Transition-Edge Sensor*, Phys. Rev. Lett. 90, 238306 (2003)

[19] G. W. Fraser: *On the nature of the superconducting-to-normal transition in transition edge sensors*, NIM A, 523, 234, (2004)

[20] M. A. Lindeman et al.:*Percolation model of excess electrical noise in transition-edge sensors*, NIM A, 559, 715, (2006)

[21] K. D. Irwin: *Thermodynamics of nonlinear bolometers near equilibrium*, NIM A, 559, 718, (2006)

[22] I. J. Maasilta and K. M. Kinnunen: *New analysis method for I-V and complex impedance data of transition-edge sensors*, to be published.

[23] M. A. Lindeman, S. Bandler, R. P. Brekosky, J. A. Chervenak, E. Figueroa-Feliciano, F. M. Finkbeiner, M. J. Li and C. A. Kilbourne: *Impedance Measurements and Modeling of a Transition-Edge-Sensor Calorimeter*, Rev. Sci. Instrum. 75 1284–1289 (2004)

[24] S. R. Elliott: *The Physics and Chemistry of Solids*, Chichester : Wiley, 1998, Repr. with corr. (2006).

[25] Range, Shannon K'doah: *Gravity Probe B: Exploring Einstein's Universe with Gyroscopes.* NASA, (2004)

[26] A. E. Mussett, M. A. Khan, S. Button: *Looking into the earth: An introduction to geological geophysics*, Cambridge University Press, (2000).

[27] J. Mehl et al.: *TES Bolometer Array for the APEX-SZ Camera*, J. Low Temp. Phys. 151, 697-702, (2008).

[28] D. Rosenberg, S. W. Nam, P. A. Hiskett, C. G. Peterson, R. J. Hughes, J. E. Nordholt, A. E. Lita, and A. J. Miller: *Quantum key distribution at telecom wavelengths with noise-free detectors*, Appl. Phys. Lett. 88, 021108, (2006).

[29] B. L. Zink, J. N. Ullom, J. A. Beall, K. D. Irwin, W. B. Doriese, W. D. Duncan, L. Ferreira, G. C. Hilton, R. D. Horansky, C. D. Reintsema, and L. R. Vale: *Array-compatible transition-edge sensor microcalorimeter γ-ray detector with 42 eV energy resolution at 103 keV*, Appl. Phys. Lett., 89, 124101, (2006).

[30] A. Luukanen, R. H. Hadfield, A. J. Miller and E. N. Grossman, *A superconducting antenna coupled microbolometer for THz applications*, Proc. SPIE Vol. 5411, Terahertz for Military and Security Applications II, (2004).

[31] A. Filipponi, A. Di Cicco, C. R. Natoli: *X-ray absorption spectroscopy and n-body distribution functions in condensed matter*, Physical review B, Vol. 52, No. 21, (1995).

[32] J. J. Rehr, R. C. Albers: *Theoretical approaches to x-ray absorption fine structure*, Reviews of Modern Physics, Vol.72, No. 3, (2000).

[33] D. E. Sayers, E. A. Stern, F. W. Lytle: *New Technique for Investigating Noncrystalline Structures: Fourier Analysis of the Extended X-Ray-Absorption Fine Structure*, Phys. Rev. Lett. 27, 1204, (1971).

[34] W. Fullagar, M. Harbst, S. Canton, J. Uhlig, M. Walczak, C. G. Wahlström, and V. Sundström: *A broadband laser plasma x-ray source for application in ultrafast chemical structure dynamics*, Rev. Sci. Instrum. 78 115105 (2007).

[35] P. G. de Gennes: *Superconductivity of Metals and Alloys*, Redwood City, CA : Addison-Wesley, (1994).

[36] J. Martinis, G. Hilton, K. Irwin, D. Wollman: *Calculation of T_c in a normal-superconductor bilayer using the microscopic-based Usadel theory*, Nucl. Instrum. Methods Phys. Res. A 444, 23 (2000).

[37] I. Maasilta, K. Kinnunen, A. Nuottajärvi, E. Kiuru, S.v Vaijärvi: *Integrated Hot-electron Bolometers Technical Note # 4: Manufacturing dossier Issue 2*, (2007).

[38] J. E. Sadleir et al.: *Bismuth X-ray absorber studies for TES microcalorimeters*, NIM A, 559, 2, (2006)

[39] K. Kinnunen, A. K. Nuottajärvi, J. Leppäniemi and I. J. Maasilta: *Reducing Excess Noise in Au/Ti Transition-Edge Sensors*, Journal of Low Temperature Physics, Vol. 151, Numbers 1-2, (2008).

[40] M. D. Niemack et al.: *A Kilopixel Array of TES Bolometers for ACT: Development, Testing, and First Light* Journal of Low Temperature Physics, Vol. 151, Issue 3-4, 690-696, (2008).

[41] P. Rai Choulhuri: *Handbook of Microlithography, Micromachining and Microfabrication, Vol 1:Microlithography*, Electronics & Communication Engineering Journal, Volume: 10, (1998).

[42] I. Brodie and J. J. Muray: *The Physics of Micro/Nano-Fabrication*, Plenum Press, New York, (1992).

[43] M. J. Madou: *Fundamentals of Microfabrication The Science of Miniaturization 2nd Edition*, CRC Press, USA, (2002).

[44] M. R. J. Palosaari: *Transitioreunasensorin toiminta ja valmistus*, Bachelor Thesis, University of Jyväskylä, (2008).

[45] S. M. Rossnagel, J. J. Cuomo and W. D. Westwood: *Handbook of Plasma Processing Technology*, New York, Noyes Publications/William Andrew Publishing, (1990).

[46] S. Franssila: *Introduction to Microfabrication*, John Wiley & Sons Ltd, Great Britain, (2004).

[47] C. Bailey (Ed.): *Advanced Cryogenics, The International Cryogenics Monograph Series*, Plenum Press, London, (1971)

[48] R. P. Welty: *Integrated SQUID Array Amplifiers*, Ph.D. Thesis, University of Colorado, (1995).

[49] A. Luukanen, H. Sipilä, K. M. Kinnunen, A. K. Nuottajärvi, and J. P. Pekola: *Transition-edge microcalorimeters for X-ray space application*, Physica B, 284-288, 2133-2134, (2000).

[50] M. A. Lindeman, S. Bandler, R. P. Brekosky, J. A. Chervenak, E. Figueroa-Feliciano, F. M. Finkbeiner, R. L. Kelley, T. Saab, C. K. Stahle, D. J. Talley: *Performance of compact TES arrays with integrated high-fill-fraction X-ray absorbers*, NIM A, 520, 411-413, (2004).

[51] T. Morooka, K. Tanaka, A. Nagata, S. Nakayama, K. Chinone, K. Futamoto, R. Fujimoto and K. Mitsuda: *High-speed superconducting x-ray calorimeter using a transition edge sensor*, Supercond. Sci. Technol. 15, 133-135, (2002).

[52] K. D. Irwin, G. C. Hilton, D. A. Wollman, and J. M. Martinis: *Thermal-response time of superconducting transition-edge microcalorimeters*, J. Appl. Phys. vol. 83, pp. 3978-3985,(1998).

[53] K. Kinnunen, M. Bruijin, H. Hovers: *XEUS CIS / WP 240 Absorber material survey*, XEUS Cryogenic Imaging Spectrometer, SRON-CIS-Rep-WP-240, Issue 4.0, (2002).

[54] F. Y. Yang, K. Liu, K. Hong, D. H. Reich, P. C. Searson, C. L. Chien: *Large Magnetoresistance of Electrodeposited Single-Crystal Bismuth Thin Films*, Science, 284. 1335 - 1337, (1999).

[55] Pobell, Frank: *Matter and Methods at Low Temperatures*, 2nd ed. Berlin, Springer, cop. (1996).

[56] E. Scheer, P. Joyez, D. Esteve, C. Urbina and M. H. Devoret: *Conduction Channel Transmissions of Atomic-Size Aluminum Contacts*, Phys. Rev. Lett. Vol. 78 Number 18, (1997).

[57] B. D. Josephson: *The discovery of tunnelling supercurrents*, Rev. Mod. Phys. Vol. 46 Number 2, (1974).

[58] P. S. de Laplace: *Théorie Analytique des Probabilités*, Paris : Mme Ve Courcier (1812).

[59] A. Niemi: *Fourier-analyysi ja Laplace-muunnos*, Jyväskylä, (2004).

[60] D. W. Jordan and P. Smith: *Mathematical Techniques*, New York, Oxford University Press, (1995).

Appendix A

Josephson Effect

Under suitable conditions so-called Josephson effects can occur, where superconducting electron pairs from a superconductor tunnel through an insulator into another superconductor [7]. This phenomenon was first suggested by Brian Josephson in 1962 [57].

A.1 DC-Josephson Effect

The time-dependent Scrödinger equation is

$$i\hbar\frac{\partial\psi}{\partial t} = H\psi, \tag{A.1}$$

where ψ is the order parameter according to Ginzburg–Landau theory, which satisfies

$$\psi(r)\psi^*(r) = n(r), \tag{A.2}$$

where $*$ refers to complex conjugate and $n(r)$ is is the local concentration of superconducting electrons. Lets define ψ_1 to be the order parameter on the one side of the system and ψ_2 on the other. Lets apply (A.1) to the two amplitudes to get two equations

$$i\frac{\partial\psi_1}{\partial t} = T\psi_2; \qquad i\frac{\partial\psi_2}{\partial t} = T\psi_1, \tag{A.3}$$

where $\hbar T$ represents the effect of the electron-pair coupling or transfer interaction across the insulator. Lets assume

$$\psi_j = n_j^{1/2}e^{i\theta_j} \qquad j = 1, 2.$$

Then

$$\frac{\partial\psi_1}{\partial t} = \frac{1}{2}n_1^{-1/2}e^{i\theta_1}\frac{\partial n_1}{\partial t} + i\psi_1\frac{\partial\theta_1}{\partial t} = -iT\psi_2; \tag{A.4}$$

$$\frac{\partial\psi_2}{\partial t} = \frac{1}{2}n_2^{-1/2}e^{i\theta_2}\frac{\partial n_2}{\partial t} + i\psi_2\frac{\partial\theta_2}{\partial t} = -iT\psi_1. \tag{A.5}$$

By multiplying (A.4) by $n_1^{1/2}e^{-i\theta_1}$ and (A.5) by $n_2^{1/2}e^{-i\theta_2}$ and defining $\delta = \theta_2 - \theta_1$ to get

$$\frac{1}{2}\frac{\partial n_1}{\partial t} + in_1\frac{\partial \theta_1}{\partial t} = -iT(n_1n_2)^{1/2}e^{i\delta}; \tag{A.6}$$

$$\frac{1}{2}\frac{\partial n_2}{\partial t} + in_2\frac{\partial \theta_2}{\partial t} = -iT(n_1n_2)^{1/2}e^{-i\delta}. \tag{A.7}$$

Now lets equate the real and imaginary parts of the equations (A.6) and (A.7) since

$$e^{i\theta} = \cos\theta + i\sin\theta :$$

$$\frac{\partial n_1}{\partial t} = 2T(n_1n_2)^{1/2}\sin\delta; \qquad \frac{\partial n_2}{\partial t} = 2T(n_1n_2)^{1/2}\sin\delta \tag{A.8}$$

$$\frac{\partial \theta_1}{\partial t} = -T(\frac{n_2}{n_1})^{1/2}\cos\delta; \qquad \frac{\partial \theta_2}{\partial t} = -T(\frac{n_1}{n_2})^{1/2}\cos\delta. \tag{A.9}$$

If $n_1 \approx n_2$ as is the case for identical superconductors 1 and 2, one now gets from (A.9) that

$$\frac{\partial \theta_1}{\partial t} = \frac{\partial \theta_2}{\partial t}; \qquad \frac{\partial}{\partial t}(\theta_1 - \theta_2) = 0. \tag{A.10}$$

From (A.8) it's clear that

$$\frac{\partial n_1}{\partial t} = -\frac{\partial n_2}{\partial t}. \tag{A.11}$$

The current flow from one superconductor to the other is proportional to $\frac{\partial n_1}{\partial t}$ or $-\frac{\partial n_2}{\partial t}$, so we may conclude that the current J of SC pair is proportional to the phase difference δ

$$J = J_0\sin\delta = J_0\sin[\theta_2 - \theta_1], \tag{A.12}$$

where J_0 is proportional to the T. Equation (A.12) tells that with no voltage applied across the junction a DC-current will flow across the junction. This is known as the DC-Josephson effect.

A.2 AC-Josephson Effect

The case is identical to the previous case but now a constant DC-voltage V is applied across the junction. This can be done due to fact that there is an insulator between the two superconductors. Now electron pair on one side is at the potential energy $-eV$ and at eV on the other side. The equations of motion now become (A.3):

$$i\hbar\frac{\partial \psi_1}{\partial t} = \hbar T\psi_2 - eV\psi_1; \qquad i\hbar\frac{\partial \psi_2}{\partial t} = \hbar T\psi_1 + eV\psi_2, \tag{A.13}$$

One can proceed as in the previous case to get following equation:

$$\frac{1}{2}\frac{\partial n_1}{\partial t} + in_1\frac{\partial \theta_1}{\partial t} = ieVn_1\frac{1}{\hbar} - iT(n_1n_2)^{1/2}e^{i\delta}. \tag{A.14}$$

The equation (A.14) again can be divided into real and imaginary parts.

$$\frac{\partial n_1}{\partial t} = 2T(n_1 n_2)^{1/2} \sin\delta, \tag{A.15}$$

which is the same as without the applied voltage V. The imagenary part is

$$\frac{\partial \theta_1}{\partial t} = \frac{eV}{\hbar} - T(\frac{n_2}{n_1})^{1/2} \cos\delta, \tag{A.16}$$

which differs from (A.9) by the term $\frac{eV}{\hbar}$. Further by extension of (A.7) one gets:

$$\frac{1}{2}\frac{\partial n_2}{\partial t} + i n_2 \frac{\partial \theta_2}{\partial t} = -i\frac{eV n_2}{\hbar} - iT(n_1 n_2)^{1/2} e^{-i\delta}, \tag{A.17}$$

whence

$$\frac{\partial n_2}{\partial t} = -2T(n_1 n_2)^{1/2} \sin\delta; \tag{A.18}$$

$$\frac{\partial \theta_2}{\partial t} = -\frac{eV}{\hbar} - T(n_1 n_2)^{1/2} \cos\delta. \tag{A.19}$$

From (A.16) and (A.19) and $n_1 \approx n_2$ one gets

$$\frac{\partial(\theta_2 - \theta_1)}{\partial t} = \frac{\partial \delta}{\partial t} = \frac{-2eV}{\hbar}, \tag{A.20}$$

which is a differential equation that can be solved easily.

$$\delta(t) = \delta(0) - \frac{2eVt}{\hbar}. \tag{A.21}$$

Now the superconducting current is

$$J = J_0 \sin[\delta_0 - \frac{2eVt}{\hbar}]. \tag{A.22}$$

From equation (A.22) one can conclude that when DC-voltage is applied the current oscillates with frequency

$$\omega = \frac{2eV}{\hbar}. \tag{A.23}$$

The phenomena is known as the AC-Josephson effect, which is utilized e.g. with SQUIDs.

Appendix B

Solving the Heat Equation

The calorimeter can be modelled with equation (2.9)

$$C\frac{\mathrm{d}T(t)}{\mathrm{d}t} = P - GT(t) + GT_{bath} + E_\gamma\delta(t).$$

The equation can be solved in a simple way by applying the Laplace transform [58]. It converts ordinary differential equations into algebra equations and thus makes them easier to solve. Laplace transform is an integral transformation and it is defined as

$$\int_0^\infty \mathrm{e}^{-st} f(t)\mathrm{d}t) = \widetilde{f}(s), \tag{B.1}$$

where $f(t)$ is the original function and $\widetilde{f}(s)$ is the transformed function. The inverse Laplace transformation is a complex integral and it is defined as

$$f(t) = \frac{1}{2\pi i}\lim_{\tau\to\infty}\int_{\gamma-i\tau}^{\gamma+i\tau} \mathrm{e}^{st}\widetilde{f}(s)\mathrm{d}s, \tag{B.2}$$

where γ is a real number so that the contour path of the integration is in the region of convergence of $\widetilde{f}(s)$. This integral is a rather nasty one and the inverse Laplace transformations of basic functions can be found in numerous books e.g. [59].

Lets now do the Laplace transformation for the equation (2.9) to get

$$Cs\widetilde{T}(s) - CT(0) = \frac{P}{s} - G\widetilde{T}(s) + \frac{GT_{bath}}{s} + E_\gamma, \tag{B.3}$$

where $T(0) = \frac{P}{G} + T_{bath}$ is initial value for T. The Laplace transformations of different functions can be found tabeled in myriad of books e.g. [60]. Lets calculate further and

try to get $\widetilde{T}(s)$ on one side of the equation and rest on the other side.

$$\begin{aligned}(CS+G)\widetilde{T}(s) &= \frac{CP}{G} + CT_{bath} + \frac{GT_{bath}}{S} + E_\delta \\ &= \frac{CPs + CGT_{bath}s + GP + G^2T_{bath} + sE_\gamma G}{sG} \\ &= \frac{s\left(CP + CGT_{bath} + E_\gamma G\right) + G(P + GT_{bath})}{sG} \\ &\Leftrightarrow \\ \widetilde{T}(s) &= \frac{s\overbrace{\left(CP + CGT_{bath} + E_\gamma G\right)}^{\alpha} + G\overbrace{(P + GT_{bath})}^{\beta}}{sCG\left(s + G/C\right)}\end{aligned}$$

Lets now do partial fractions trick and set

$$\begin{aligned}\widetilde{T}(s) &= \frac{s\alpha + G\beta}{sCG\left(s + \frac{G}{C}\right)} = \frac{A}{sCG} + \frac{B}{s + G/C} \\ &= \frac{s\left(A + GCB\right) + G/CA}{sCG(s + G/C)}\end{aligned}$$

so

$$\begin{aligned}A + CGB = \alpha \text{ and } A/C = B \\ \Rightarrow \\ C\beta + CGB = \alpha \\ \Leftrightarrow \\ B &= \frac{\alpha - C\beta}{CG} \\ &= \frac{C\beta + E_\gamma G - CB}{CG} \\ &= \frac{E_\gamma}{C}\end{aligned}$$

therefore

$$\begin{aligned}\widetilde{T}(s) &= \frac{P + GT_{bath}}{sG} + \frac{E_\gamma/C}{s + G/C} \\ &= \frac{1}{s}\left(\frac{P}{G} + T_{bath}\right) + \frac{E_\gamma}{C}\frac{1}{s + G/C}\end{aligned}$$

Now by doing the inverse Laplace transform to this we finally get the solution (2.10)

$$T(t) = \frac{E_\gamma}{C}\mathrm{e}^{-\frac{G}{C}t} + P/G + T_{bath}.$$